Geophysical Journal International

Geophys. J. Int. (2022) **231,** 877–893
Advance Access publication 2022 May 31
GJI Seismology

https://doi.org/10.1093/gji/ggac196

Kinetic effects on the 660-km-phase transition in mantle upstreams and seismological implications

Stephan Lessing,[1,*] David P. Dobson,[2] Sebastian Rost,[3] Laura Cobden[1,4] and Christine Thomas[1]

[1]*Institute of Geophysics, Westfälische Wilhelms-Universität Münster, Corrensstraße* 24, 48149 *Münster, Germany, E-mail: stephan.lessing@outlook.de*
[2]*Department of Earth Sciences, University College London, Gower Street, London WC*1*E* 6*BT, United Kingdom*
[3]*School of Earth and Environment, Institute of Geophysics and Tectonics, University of Leeds, Leeds LS*29*JT, United Kingdom*
[4]*Department of Earth Sciences, Utrecht University, Princetonlaan* 8*a,* 3584*CB Utrecht, The Netherlands*

Accepted 2022 May 24. Received 2022 May 16; in original form 2022 February 5

SUMMARY

The effects of reaction kinetics of bridgmanite and ferropericlase transforming to ringwoodite on elastic properties in upwelling mantle are investigated using data of kinetic experiments and internally self-consistent thermodynamic modelling of density and seismic velocities. The kinetic experiments show inhibited grain growth of ringwoodite. At the initiation of ringwoodite growth, bridgmanite completely transforms to a metastable pyrope-bearing garnet. Ringwoodite then gradually grows from the metastable assemblage of ferropericlase and garnet. The changes in mineralogy result in a low-velocity zone directly above the 660 km seismic discontinuity due to the lower seismic velocities and densities of ferropericlase and garnet compared to ringwoodite and bridgmanite. The modelling of the effects of reaction kinetics and its effect on seismic structure at ∼660 km depth shows more sensitivity to grain size than to temperature and upwelling rate. Modelling 1-D synthetic seismograms of PP (SS) underside reflections off the kinetically inhibited backward reaction to ringwoodite shows advanced traveltimes of underside reflections off ∼660 km depth of 0.2–0.8 s (1.2–1.6 s) for upwelling rates of 50 cm yr^{-1} and initial grain sizes between 5 and 20 cm due to the low-velocity zone above the 660 km discontinuity. The finite width of the low-velocity layer results in frequency-dependent behaviour of PP and SS underside reflection amplitudes, with higher amplitudes towards shorter periods. The effect on the traveltimes of P-to-s conversions used for receiver function is small (<0.7 s) but the inhibited backward reaction leads to strong amplitude changes and significant waveform variations. The effects of reaction kinetics in mantle upwellings might serve as an additional means to map regions of large-scale upwellings and to constrain grain size in the lower mantle.

Key words: Composition and structure of the mantle; High-pressure behaviour; Phase transitions; Body waves.

1 INTRODUCTION

The seismic structure of the Earth's mantle transition zone between upper and lower mantle is dominated by two seismic discontinuities at which the seismic velocities and density increase over short depth intervals. These discontinuities are found in most spherically averaged 1-D Earth reference models, for example ak135 (Kennett *et al*. 1995), and are considered as the seismic expressions of solid–solid phase transitions and mineral reactions (both hereafter called phase transformations) of the olivine system (e.g. Ringwood 1969; Helffrich 2000; Shearer 2000; Weidner & Wang 2000; Deuss 2009). Thermodynamic calculations of mantle mineral phase relations are frequently used to interpret observations of seismic velocities and seismic discontinuity structure and help to identify and quantify their thermal and compositional origins (e.g. Cobden *et al*. 2008; Ritsema *et al.* 2009; Saki *et al*. 2019; Waszek *et al*. 2021).

For thermodynamic modelling of phase equilibria and their seismic properties, the Earth's mantle is usually assumed as vigorously convecting, homogeneous and well mixed. However, geodynamic studies have demonstrated the long-term existence of thermal and compositional heterogeneities throughout the mantle (e.g. Allègre & Turcotte 1986; Kellogg *et al*. 2002; Tackley *et al*. 2005; Ballmer *et al*. 2017). Small diffusivities of the solid mantle (e.g. Hofmann &

*Now at: Ferchau GmbH, Branch Office Bremen-City, Lloydstraße 4/6, 28217 Bremen, Germany.

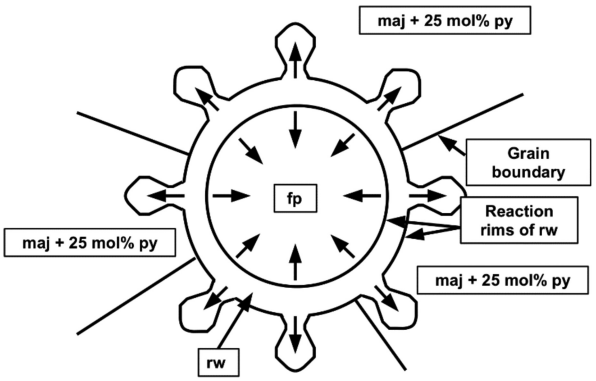

Figure 1: Sketch of the reaction mechanism for the recombination of bridgmanite and ferropericlase (fp) to ringwoodite (rw). The ringwoodite layer nucleates on the fp grain surface and grows into majorite garnet (maj) which contains 25 mol per cent Al-bearing pyrope (py) in a fingering instability. After Dobson & Mariani (2014).

Table 1: Pyrolite composition by Sun *et al*. (1982) used in this study. The oxides of the CFMAS system are given as molar percentages.

SiO_2	MgO	Al_2O_3	FeO	CaO
38.61	49.13	2.77	6.24	3.25

Hart 1978; Farber *et al*. 1994) lead to the question: to what degree have the mineral assemblages reached thermodynamic equilibrium and mineral transformations been completed? The mechanisms of mineral transformations, that is their reaction kinetics, might therefore affect the dynamics and seismic structure of the Earth's mantle (e.g. Kubo *et al*. 2002, 2008). Therefore, taking the reaction kinetics into account might be essential for our interpretation of the seismic signals in terms of mantle composition and temperature.

The influence of reaction kinetics on mineral transformations was first investigated in detail when seismologists looked for mechanisms of deep earthquakes in subducting slabs (e.g. Sung & Burns 1976; see Kirby *et al*. 1996, for a review). Motivated by observations of apparently stagnant slabs at ∼660 km depth in seismic tomography models (e.g. van der Hilst 1991; Fukao *et al*. 2001, 2009) Kubo *et al*. (2002, 2008) investigated the reaction kinetics of phase transformations of ringwoodite to ferropericlase and bridgmanite and of garnet to bridgmanite at ∼660 km depth and temperature conditions typical for subducting slabs. The kinetic experiments by Kubo *et al*. (2002, 2008) show that low temperatures within the slab decrease the mobility of atoms in the crystal lattice and hence could reduce reaction rates of mineral transformations. The kinetic inhibition of the phase transformations of ringwoodite to ferropericlase and bridgmanite and of garnet to bridgmanite result in neutral to positive buoyancy which may lead to stagnant slabs. Recently it has also been shown that kinetics of the bridgmanite to post-perovskite phase transition can affect visibility of the *D*" reflector (Langrand *et al*. 2019).

Reaction mechanisms of mineral transformations can also change for higher temperatures. Studies by Gasparik (1996a, b), Weidner & Wang (1998), Irifune *et al*. (1998) and Hirose (2002) show that the reaction mechanism of ringwoodite to ferropericlase and bridgmanite changes for mantle temperatures larger than 2100 K. This temperature is considered as a reasonable estimate for the centre of hot mantle upwellings (e.g. Sleep 1990; Schilling 1991; Weidner & Wang 1998). For aluminium contents of approximately 5 wt per cent and temperatures of at least 2100 K, ringwoodite transforms to bridgmanite and ferropericlase via the dissociation of ringwoodite to ferropericlase and majorite garnet, and finally to ferropericlase and bridgmanite (Gasparik 1996a, b; Irifune *et al*. 1998; Weidner & Wang 1998; Hirose 2002).

Kinetic studies by Shimojuku *et al*. (2014) and Dobson & Mariani (2014) have investigated the reaction kinetics for the reverse reaction of bridgmanite and ferropericlase to ringwoodite in upwelling mantle. The kinetic experiments show that the growth of ringwoodite is kinetically inhibited, and that bridgmanite transforms to pyrope-bearing garnet. The reverse reaction from bridgmanite and ferropericlase to ringwoodite and garnet (in mantle upwellings) requires diffusion on a much larger length-scale than the forward reaction because macroscopic grains of bridgmanite and ferropericlase must recombine to form ringwoodite (Dobson & Mariani 2014). In the case of aluminous garnets, the interface between ringwoodite and garnet develops a fingering instability resulting in a complex intergrowth (Fig. 1). Garnet incorporates the aluminium oxide of the bridgmanite into its crystal lattice and has the same bulk chemistry as the bridgmanite before the transformation, and hence this isochemical transformation is fast compared to the diffusion-controlled reaction between bridgmanite and ferropericlase. Over time, this chemically metastable garnet reacts with ferropericlase, and the stable phase, ringwoodite, starts to nucleate and grow at the interface between ferropericlase and garnet.

The growth of ringwoodite on the ferropericlase grains is most likely controlled by the slow diffusion of SiO_2 from garnet across the reaction layer into the grains of ferropericlase. The ringwoodite growth rate is sensitive to the initial grain size of lower mantle minerals (Dobson & Mariani 2014). The initial ferropericlase grain size is the typical length scale of diffusion. The amount of ringwoodite formed depends on bulk composition and ambient temperature. The bulk composition affects the individual molar amounts of the mineral solid solutions. The ambient mantle temperature influences the equilibrium phase relations and mobility of atoms, determining the diffusion rate of atoms across interfaces and grain boundaries (e.g. Putnis 1992). The initial grain size controls the relative proportions of reactants and products for a given amount of diffusion across the reacting interface.

Our study investigates the effects of reaction kinetics for the recombination of bridgmanite and ferropericlase to ringwoodite in mantle upwellings on density and seismic wave velocities to assess the possibility to observe the effects of the kinematically inhibited back reaction seismically. The kinetically inhibited growth of ringwoodite is determined for a range of mantle temperatures at 660 km depth, varying grain sizes and mantle upwelling rates. The changed volume fractions of the minerals as a function of pressure are used to calculate profiles of density, *P*- and S-wave velocities for kinetically inhibited and equilibrated phase assemblages using internally self-consistent thermodynamic modelling. These models are used to compute 1-D synthetic seismograms for PP and SS underside reflections off the resulting discontinuity and for P-to-s conversions at the discontinuity (known as P receiver functions), two probes often used to study upper mantle discontinuities, to assess the effects on traveltimes and waveforms. Our aim is not to carry out a seismic study at this point to search for such effects in observed seismic data. This work presents a previously unstudied effect of mantle phase transitions on seismic data that should be kept in mind in future seismic studies.

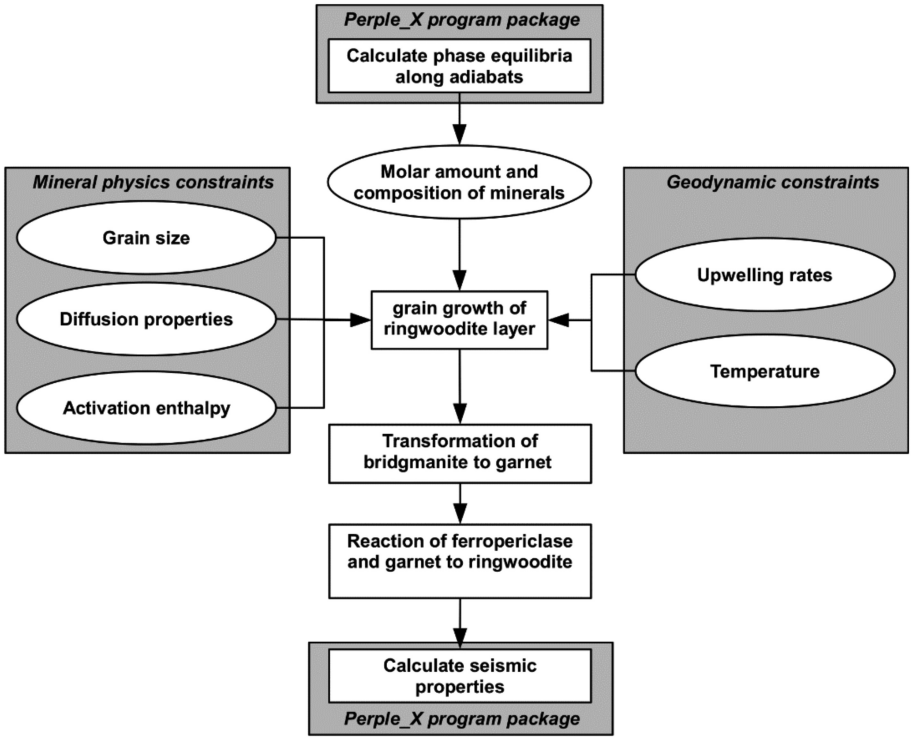

Figure 2: Forward modelling of seismic properties for kinetically inhibited growth of ringwoodite and corresponding mineral reactions for ferropericlase, bridgmanite and garnet.

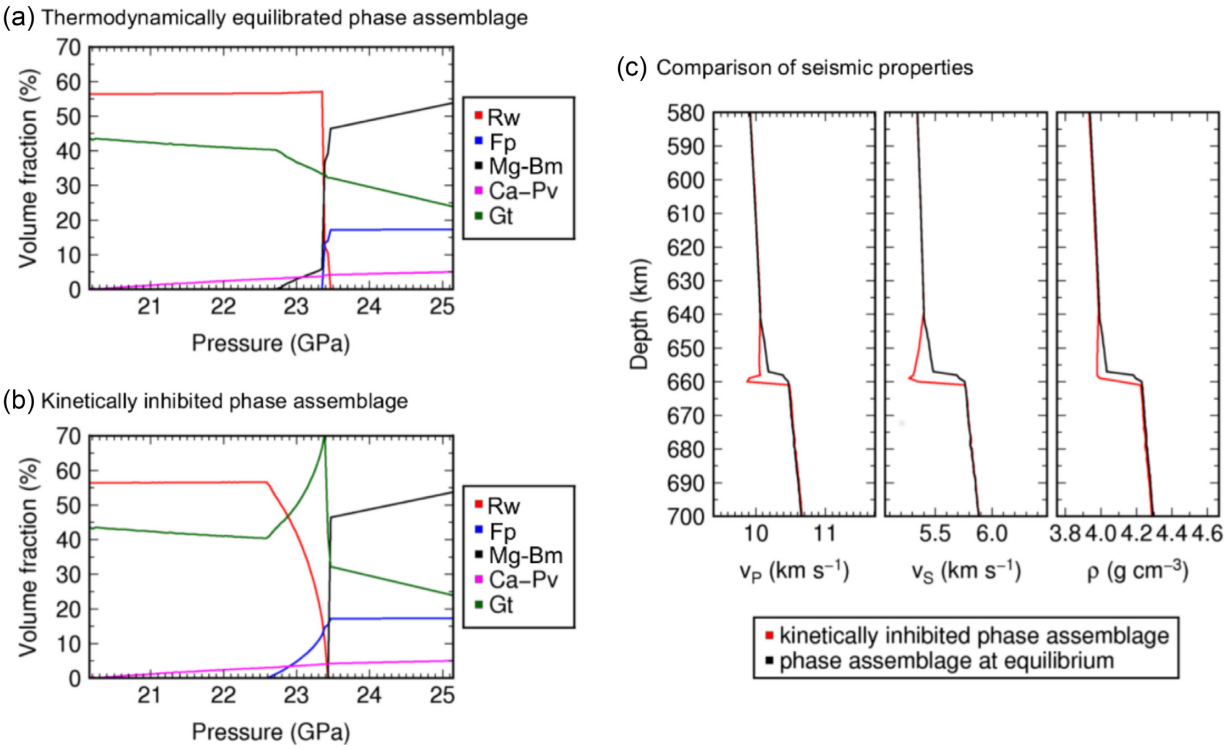

Figure 3: Example for effects of kinetic inhibition of ringwoodite growth on volume fractions of minerals and on seismic properties of phase assemblages for temperature of 1850 K (following the 1300 °C adiabat), 5 cm initial grain size and 50 cm yr^{-1} upwelling rate. (a) Volume fractions of equilibrated phase assemblages as a function of pressure for pyrolite composition along the 1300 °C adiabat. Mineral phases are abbreviated as follows: Rw: ringwoodite, Fp: ferropericlase, Mg-Bm: magnesium bridgmanite, Ca-Pv: calcium perovskite, Gt: garnet. (b) Volume fractions of kinetically inhibited phase assemblages as a function of pressure for pyrolite composition along the 1300 °C adiabat. (c) Comparison of seismic velocities and density between equilibrated and kinetically inhibited phase assemblages.

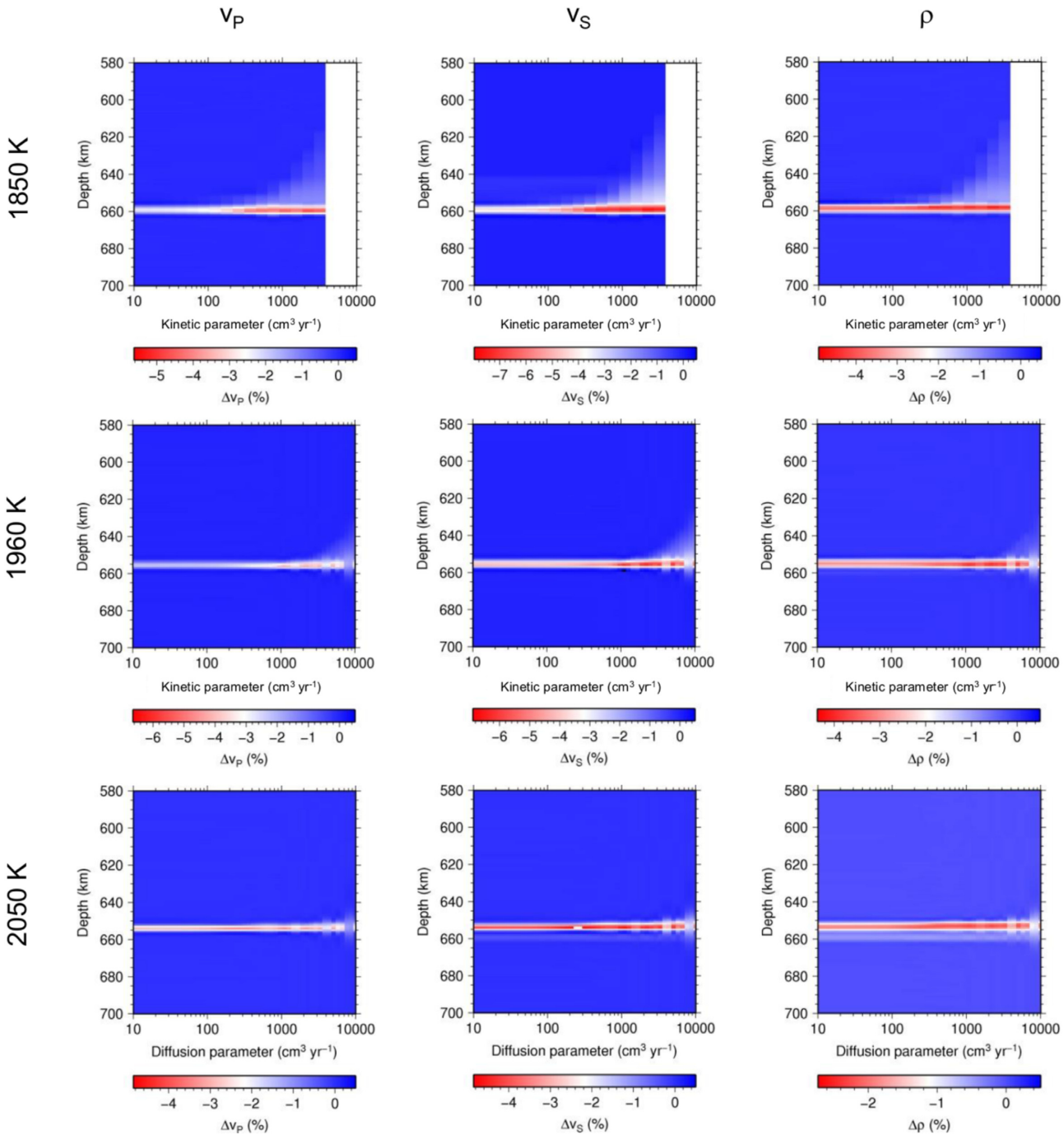

Figure 4: Relative differences of *P*-wave velocity, *S*-wave velocity and density due to the kinetically inhibited growth of ringwoodite and the presence of metastable ferropericlase and garnet for temperatures of 1850, 1960 and 2050 K. No data are available for kinetic parameters >4000 cm^3 yr^{-1} because the ringwoodite growth interferes with the ringwoodite-to-wadsleyite transition. To date, no studies with kinetic data for the ringwoodite-to-wadsleyite transition in mantle upstreams are known to the authors.

Table 2: Relationship between surface potential temperature of a mantle adiabat and their ambient temperatures at ∼23.4 GPa, that is at ∼660 km depth. Surface potential temperature are often given in °C (e.g. Cammarano *et al*. 2005; Cobden *et al*. 2008) whereas ambient temperatures are usually given in K.

Potential temperature (°C)	1300	1400	1500
Ambient temperature (K)	1850	1960	2050

2 METHODS

The kinetically inhibited growth of ringwoodite and its effects on phase assemblages and seismic properties are computed in five steps:

(i) Calculation of phase equilibria.

(ii) Calculation of the thickness of the ringwoodite layer produced for a given temperature, grain size and mantle upwelling rate.

Table 3: Parameter range for calculating the seismic properties of kinetically inhibited phase assemblages.

Parameter	Value (s)
From the kinetic experiments by Dobson & Mariani (2014):	
Enthalpy of the reaction ΔH_a (kJ mol^{-1})	456±40
Diffusion coefficient ln(k_0) (m^2 s^{-1})	-6.36±0.25
For modelling seismic properties	
Temperatures (K)	1850, 1960, 2050
Grain size (cm)	1, 5, 10, 20
Upwelling rate (cm yr^{-1})	1, 5, 10, 50, 100

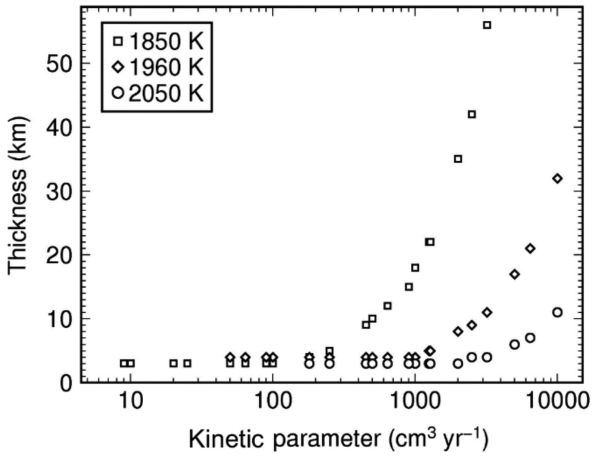

Figure 5: Thickness of the reaction interval where ringwoodite grows from the recombination of ferropericlase and garnet as function of the kinetic parameter D. The kinetic parameter D is proportional to the upwelling rate v and the square of grain size d, for simplicity we set the proportion factor to unity so that $D = v\ d^2$. Scenarios which have different grain size and upwelling rates, but have the same kinetic parameter, show the same kinetic inhibition.

(iii) Mass balancing consumption of metastable ferropericlase and garnet.

(iv) Calculation of density and seismic wave velocities.

(v) Computation of 1-D synthetic seismograms.

2.1 Calculation of phase equilibria

Phase equilibria for the CFMAS (calcium oxide, iron(II) oxide, magnesium oxide, aluminium oxide and silica) system are calculated for a pyrolitic mantle composition (Table 1) with the Perple_X program package (Connolly 2005) that utilizes the free-energy minimization algorithm by Ita & Stixrude (1992) and Stixrude & Lithgow-Bertelloni (2005), and the elastic and thermodynamic properties and the solid solution model of Stixrude & Lithgow-Bertelloni (2011). From the calculated phase equilibria, profiles of *P*-wave velocity, *S*-wave velocity and density are extracted along adiabatic mantle geotherms (e.g. Cobden *et al*. 2008). The values of *P*-wave velocity, *S*-wave velocity and density of the phase assemblage at a specific P-T-point are calculated as the Hill average of Voigt and Reuss bounds of the constituent minerals (Voigt 1928; Reuss 1929; Hill 1965).

2.2 Kinetically inhibited growth of ringwoodite and mineral reactions

The seismic structures of the kinetically inhibited phase assemblages are calculated from the grain growth of ringwoodite for fixed temperature, grain size and upwelling rate (Fig. 2). Before we describe the calculations of kinetically inhibited growth of ringwoodite and its impact on seismic properties, we compare the mineral reactions at thermodynamic equilibrium with those observed by Dobson & Mariani (2014).

The recombination reaction at thermodynamic equilibrium is described as

$$MgO + MgSiO_3 \leftrightarrow Mg_2SiO_4$$

$$\text{ferropericlase} + \text{bridgmanite} \leftrightarrow \text{ringwoodite} \quad (1)$$

Dobson & Mariani (2014) observe in the kinetic experiments that bridgmanite entirely transforms to garnet, where the aluminium-bearing bridgmanite transform to pyrope garnet:

$$3.75MgSiO_3 \cdot 0.25Al_2O_3 \leftrightarrow 0.75Mg_4Si_4O_{12} + 0.25Mg_3Al_2Si_3O_{12}$$

$$\text{aluminous bridgmanite} \leftrightarrow \text{majorite garnet} + \text{pyrope garnet} \quad (2)$$

The consumption of bridgmanite to ringwoodite comprises of several reactions. At the onset of ringwoodite growth, the entire amount of bridgmanite transforms to garnet,

$$MgSiO_3 \rightarrow 0.25Mg_4Si_4O_{12},$$

$$\text{bridgmanite} \rightarrow \text{majorite garnet} \quad (3)$$

creating an excess of garnet compared to conditions at thermodynamic equilibrium.

The difference between the decrease of ferropericlase with kinetic inhibition effects and the phase fraction of ferropericlase is later used to infer the decrease of garnet which recombines with ferropericlase to give ringwoodite via the reaction

$$MgO + 0.25Mg_4Si_4O_{12} \leftrightarrow Mg_2SiO_4$$

$$\text{ferropericlase} + \text{majorite garnet} \leftrightarrow \text{ringwoodite} \quad (4)$$

The kinetically inhibited growth of ringwoodite and the dependent mineral transformations of bridgmanite and garnet are assumed to leave calcium-bearing garnets and the exsolution of calcium perovskite unaffected. Therefore, amounts of calcium-bearing garnets and calcium perovskite are extracted from the thermodynamic calculations.

We now derive how we calculate the growth kinetics of ringwoodite and account for the mineral reactions mentioned above. The growth kinetics of ringwoodite are controlled by two parameters which are determined in experiments: its enthalpy ΔH_a and its reaction rate constant k_0 which is closely linked to the reaction entropy ΔS_a.

For a mineral transformation from mineral assemblages A and B to a mineral assemblage C, the reaction rate is proportional to the molar concentrations of mineral phases A and B, C_A and C_B (Putnis 1992):

$$\text{Reaction rate proportional } K^* C_A C_B \quad (5)$$

In our case, C_A and C_B are the concentration of ferropericlase and majorite garnet.

The equilibrium constant of the reaction K^* is a function of the change of reaction Gibbs free energy, ΔG_a,

$$K^* = \exp(-\Delta G_a/(RT)) = \exp(\Delta S_a/R)\exp(-\Delta H_a/(RT)) \quad (6)$$

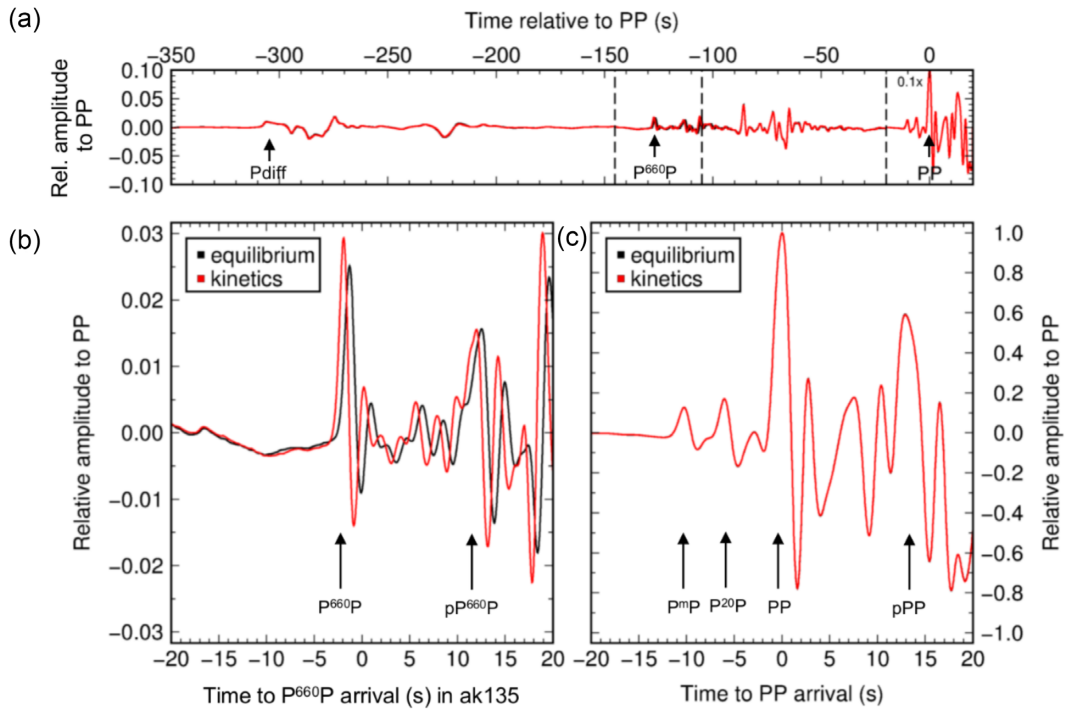

Figure 6: Synthetic seismograms of PP precursors with a dominant period of 3 s from seismic models of equilibrated and kinetically inhibited phase assemblages at an array with reference epicentral distance of 120 deg, a temperature of 1850 K, grain size of 5 cm and a vertical upwelling rate of 50 cm yr $^{-1}$. Panel (a) shows the linearly stacked traces of all calculated seismograms for equilibrated pyrolite phase assemblages (black) and kinetically inhibited phase assemblages (red) aligned with slowness for PP from ak135 (Kennett *et al.* 1995). Time windows around the predicted arrivals of P660P and PP from ak135 shown (b) and (c) and are marked by vertical lines and the phase names. Arrows indicate the arrivals of P660P and pP660P in zoomed diagram (b) and the arrivals of PP and pPP in zoomed diagram (c).

using the definition of the reaction Gibbs free energy $\Delta G_a = \Delta H_a - T\Delta S_a$ with the enthalpy of the reaction ΔH_a and the entropy of the reaction ΔS_a. R denotes the gas constant and T is temperature. The reaction rate can be rewritten as

$$\text{Reaction rate} = c\exp(\Delta S_a/R)\exp(-\Delta H_a/(RT))C_A C_B, \quad (7)$$

where c is a constant. As the concentration of the reactants changes during the reaction, the reaction rate will change accordingly. The reaction rate thus becomes a function of the phase fraction C

$$\text{Reaction rate} = kf(C) \quad (8)$$

where the reaction rate parameter k describes how the reaction rate depends on the concentration of the reactants. Therefore, the rate constant is

$$k = k(T) = c\exp(\Delta S_a/R)\exp(-\Delta H_a/(RT)) = k_0\exp(-\Delta H_a/(RT)) \quad (9)$$

with the reaction rate constant $k_0 = c\exp(\Delta S_a/R)$, where c is an experimentally determined factor.

Dobson & Mariani (2014) show that the growth kinetics of ringwoodite are controlled by diffusion kinetics. In this case, the rate of growth of the interface is linear with the square-root of time and the thickness of reaction rims measured at each temperature can be converted into apparent rate constants (Watson & Price 2002). Following Tammann (1920) and Watson & Price (2002), the temperature dependent rate constant $k(T)$ is given by

$$k(T) = \frac{1}{2}\frac{\mathrm{d}}{\mathrm{d}t}x^2, \quad (10)$$

where x is the thickness of the growing interface and t is time. Integration of (10) gives the interface thickness evolution as a function of time and temperature:

$$x(t, T) = \left((2k(T)t)^{1/2}\right). \quad (11)$$

To model the kinetic inhibition of ringwoodite growth, the interface grows until reaching the assumed initial grain size d. In this study, radially isotropic growth of the ringwoodite interface is assumed. We therefore normalize the ringwoodite interface thickness evolution (11) with half of the desired grain size (d) which results in a relative grain size:

$$x_{\text{rel}}(t, T) = \left((2k(T)t)^{1/2}\right)/(0.5d). \quad (12)$$

Since temperatures are approximately constant along the chosen adiabats, we assume a constant temperature T_0 during the reaction:

$$x_{\text{rel}}(t) = \left((2k(T_0)t)^{1/2}\right)/(0.5d). \quad (13)$$

Due to its inverse dependency on grain size d, eq. (13) indicates that growth of ringwoodite takes more time in case of large grain size.

Assuming an upwelling rate v and utilizing the depth-to-pressure scale used by Cobden *et al.* (2008), the time of grain growth is converted to a grain growth curve as a function of pressure, $x_{\text{rel}}(P)$. In our calculations, upwelling rates in the mantle are estimated to range between 1 and 100 cm yr^{-1} considering current heat flux estimates in upwelling mantle (e.g. Sleep 1990; Courtillot *et al.* 2003) and geodynamic modelling experiments (Farnetani & Hofmann 2010).

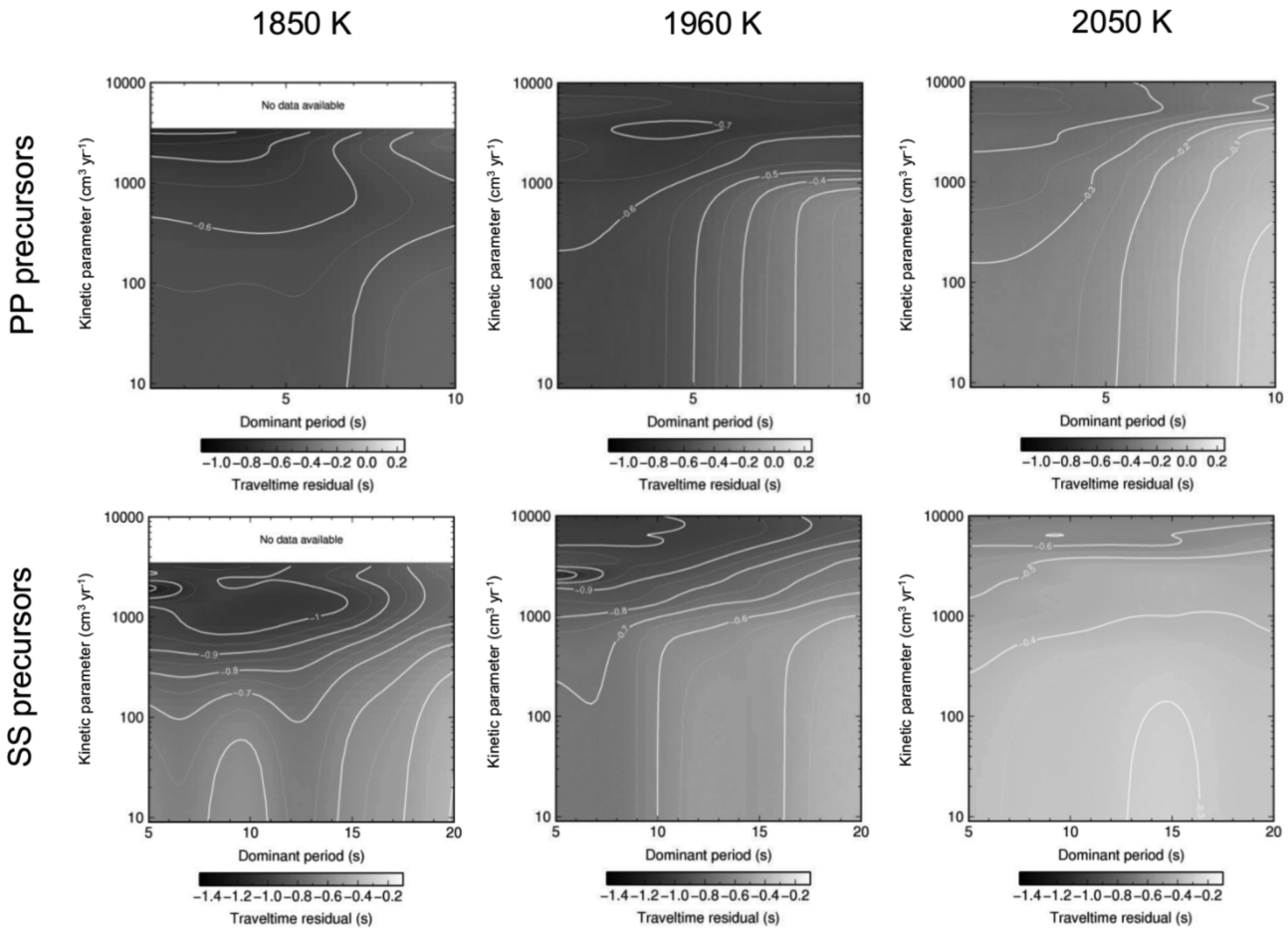

Figure 7: Traveltime residuals of stacked PP and SS precursors between kinetically inhibited and equilibrated backward reaction to ringwoodite as a function of temperature and kinetic parameter for varying dominant periods at an epicentral distance of 120 °C. Bold lines denote changes of traveltime residuals by 0.1, thin lines denotes changes of traveltime residuals by 0.05. Data are not available at temperature of 1850 K and kinetic parameters >4000 cm^3 yr^{-1} (*cf.* Fig. 4).

The average grain size in the lower mantle is estimated to range between 1 μm (Yamazaki *et al*. 1996) and 10 cm (Solomatov 1996; Korenaga 2005) based on varying estimates of grain growth kinetics of mineral transformations in downwelling, or primordial, mantle. In the interior of a subducting slab, Yamazaki *et al*. (1996) and Yamazaki *et al*. (2005) find very slow grain growth rates for ferropericlase and bridgmanite, with grain sizes ranging between 10 and 100 μm for temperatures typical for subduction zones and for 10 Myr after grain nucleation, but Fei *et al*. (2021) find a much smaller grain size exponent compared to Yamazaki *et al*. (1996). Their estimate for grain size in subducted slabs is on the order of 30–45 μm. Solomatov *et al*. (2002) question estimates of grain size for the bulk mantle as they cannot be reconciled with viscosity models or laboratory data for other materials. Solomatov *et al*. (2002) argue that the experiments have not been run sufficiently long to evaluate grain growth kinetics beyond transient effects. Solomatov (1996) and Korenaga (2005) have additionally suggested that deep-mantle plumes might have a significantly larger grain size than the ambient lower mantle due to (i) the temperature of the source region of the mantle upwelling, (ii) the kinetics of grain growth from an early magma ocean and (iii) seismic tomographic imaging of wide slow structures which have been interpreted as wide plume roots (French & Romanowicz 2015).

2.3 Mass balancing consumption of metastable ferropericlase and garnet

We follow the workflow in Fig. 2 to calculate volume fractions of the mineral phases affected by the kinetically inhibited growth of ringwoodite for given grain size d, upwelling rate v and constant temperature T_0. Ringwoodite starts to grow at pressure P_{Start} where the molar amount of ringwoodite is non-zero in the equilibrium phase assemblage. The kinetically inhibited growth of ringwoodite is calculated as the convolution of the grain growth curve and the derivative of the molar amounts of ringwoodite at thermodynamic equilibrium as a function of depth. The growth curve x_{rel} is truncated where the relative growth of ringwoodite equals 1. At this pressure, hereafter called P_{end}, the molar amount of ringwoodite with kinetically inhibited growth conditions is considered to be equal to the amount of ringwoodite at thermodynamic equilibrium. Using the molar amount of ringwoodite at P_{end}, $n_{\mathrm{Rw,end}}$, we convert the grain growth curve (12) into molar amount of ringwoodite:

$$n_{\mathrm{Rw}}(P) = n_{\mathrm{Rw,end}} x_{\mathrm{rel}}(P). \tag{14}$$

We calculate the mass balances of ferropericlase, majorite garnet and pyrope garnet, following the mineral reactions in (2)–(4). Using

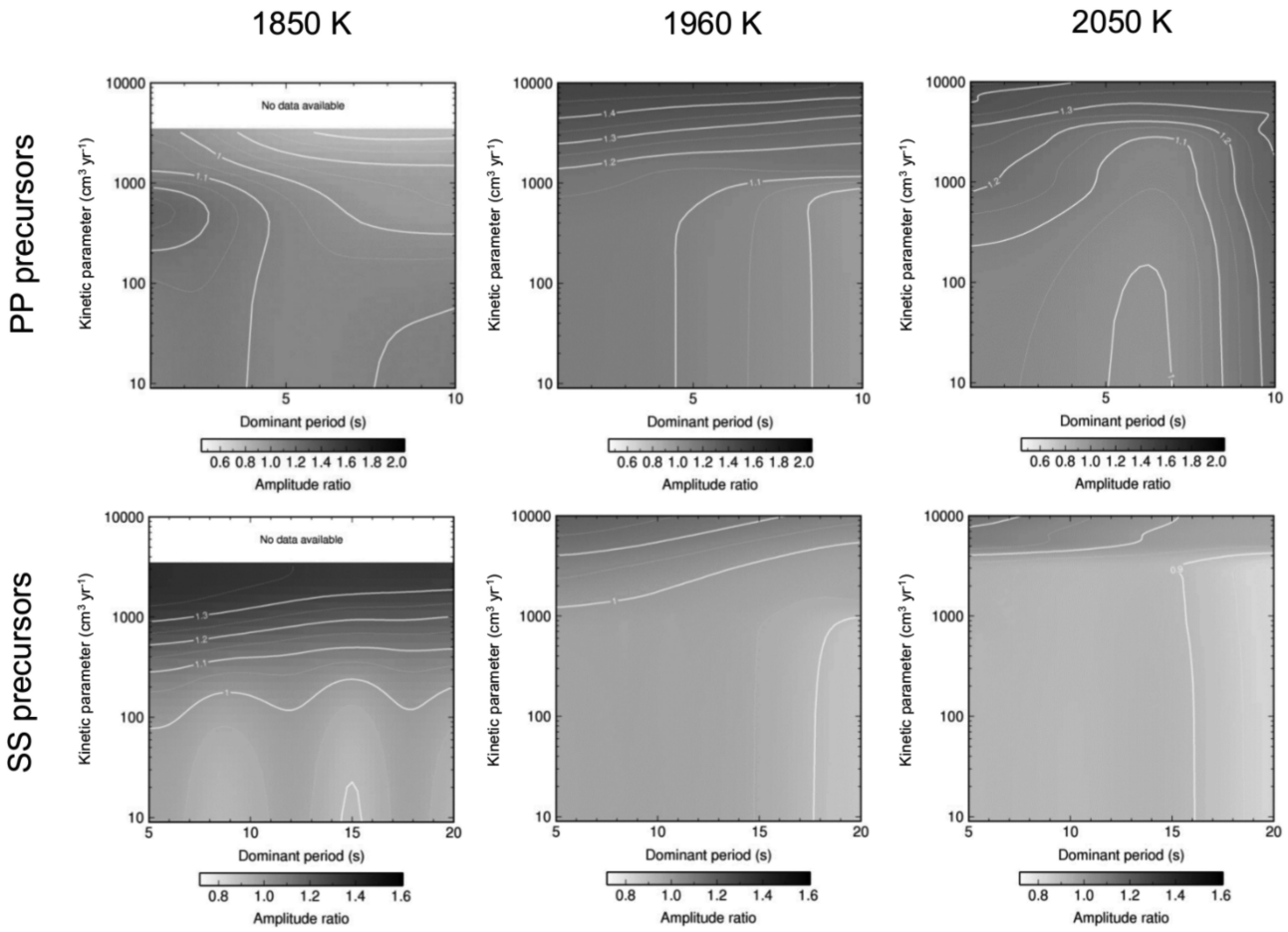

Figure 8: PP and SS precursor amplitude ratios of reflections off the kinetically inhibited reaction versus off the equilibrated reaction to ringwoodite as a function of temperature and kinetic parameter for varying dominant periods at an epicentral distance of 120°. Bold lines denote changes of amplitude ratios by 0.1, thin lines denote changes of amplitude ratios by 0.05. Data are not available at temperature of 1850 K and kinetic parameters >4000 cm^3 yr^{-1} (cf. Fig. 4).

molar volumes of the individual mineral phases from our thermodynamic calculations in section 2.1, we convert molar amounts to volume fractions within the pressure interval from P_{end} to P_{start}.

2.4 Calculation of density and seismic wave velocities

Utilizing their volume fractions calculated as described in Section 2.3, we calculate the seismic properties of the kinetically inhibited phase assemblages, for the Hill average of Voigt and Reuss bounds of the constituent minerals (Voigt 1928; Reuss 1929; Hill 1965). For each mineral, the density and seismic velocity are determined at the given pressure and temperature. The seismic properties of the kinetically inhibited phase assemblages are fit to the seismic profiles of phase assemblages at thermodynamic equilibrium for the corresponding adiabatic mantle geotherm.

2.5 Computation of 1-D synthetic seismograms

The mineral physical results can be used to test if the effects of the kinetically inhibited transformation of bridgmanite and ferropericlase to ringwoodite can be observed in seismological data. We focus on effects of PP and SS underside reflections and P-to-s conversions as they are commonly used probes to study upper mantle discontinuities. For this, the computed profiles of density, *P*-wave and *S*-wave velocity for equilibrated and kinetically inhibited phase assemblages are used to calculate 1-D reflectivity synthetic seismograms (Fuchs & Müller 1971; Müller 1985) for a range of dominant periods. Attenuation values are taken from PREM (Dziewonski & Anderson 1981). For comparison, 1-D reflectivity synthetic seismograms using the 1-D velocity model ak135 (Kennett *et al*. 1995) and attenuation of PREM (Dziewonski & Anderson 1981) are computed. Dominant periods of PP underside reflections are 1, 3, 5, 8 and 10 s. A source at 50 km depth is chosen and the data are analysed on the vertical component. For SS underside reflections, dominant periods are 5, 8, 10, 15 and 20 s. The source is at 50 km depth and the data are analysed on the transverse component. 21 receivers are distributed as a linear array around 120° epicentral distance with an aperture of 5°. An epicentral distance of 120° is within typical distances used for PP and SS precursor studies (e.g. Shearer 1991; Deuss 2009; Thomas & Billen 2009). The seismograms are aligned on the PP/SS arrival and are normalized to unit amplitude.

For the P-to-s conversions we use dominant periods of 0.5, 1 and 2 s with a source depth of 2 km to avoid interference of the P660s (and P410s for reference) arrivals with depth phases. We use a linear array with 1° receiver spacing between 40° and 80°. We calculate three-component seismograms (*Z*, *R*, *T*) but only analyse the radial component. Due to the simple source time function and the consistent waveforms, we abstain from deconvolving the vertical

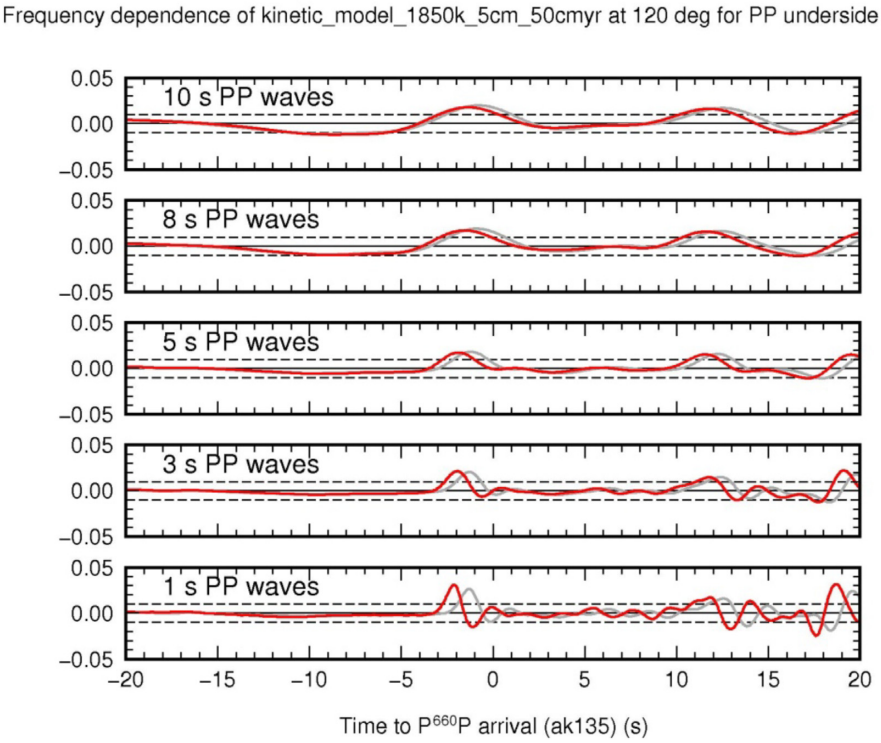

Figure 9: Frequency dependence of $P^{660}P$ underside reflections for equilibrated and kinetically inhibited phase assemblages at 1850 K, for 5 cm grain size and 50 cm yr^{-1} upwelling rate for dominant periods of 1–10 s. Waveforms of reflections off the kinetically inhibited backward reaction to ringwoodite are depicted in red, whereas waveforms of reflections off the equilibrated backward reaction to ringwoodite are depicted in black.

component *P* wave and interpret the relevant waveform variation in Section 3.

3 RESULTS

3.1 Effects of kinetic inhibition on seismic fine structure

The effects of kinetic inhibition on phase assemblages are compared with phase assemblages at thermodynamic equilibrium with regard to the mineral proportions and seismic properties. The kinetically inhibited growth of ringwoodite and the metastable assemblage of ferropericlase and pyrope-bearing garnet change the phase proportions above the onset depth of the phase transformation (Fig. 3). For equilibrated phase assemblages at a temperature of ∼1850 K (following the adiabat with 1300 °C potential surface temperature, abbreviated hereafter as '1300°C adiabat'; please see Table 2 and Cobden *et al*. 2008 for details), ringwoodite dissociates to ferropericlase and bridgmanite within a pressure interval of ∼0.1–0.2 GPa (i.e. ∼2 km) at ∼23.4 GPa (i.e. at ∼659 km depth, Fig. 3a). The amount of garnet decreases due to the exsolution of bridgmanite, starting at ∼22.7 GPa (∼642 km).

The thickness of inhibited growth of ringwoodite is sensitive to temperature, grain size and mantle upwelling rate. For 5 cm grain size and 50 cm yr^{-1} upwelling rate, the kinetic inhibition leads to a growth of ringwoodite over a pressure interval of 1 GPa (∼25 km, Fig. 3b). The gradual growth of ringwoodite results in a gradual consumption of ferropericlase. At the pressure where ringwoodite starts to grow, the entire amount of bridgmanite reacts to garnet, thus its volume fraction increases to 70 per cent. The recombination reaction of garnet and ferropericlase to ringwoodite gradually decreases the amount of garnet towards lower pressures.

The excess of garnet changes the seismic structure around 660 km depth (Fig. 3c). Since garnet has lower *P*- and *S*-wave velocities (garnet: $v_p \approx 9.8$ km s^{-1}, $v_s \approx 5.2$ km s^{-1} at 23.4 GPa and 1850 K) than ringwoodite and bridgmanite (ringwoodite: $v_p \approx 10.2$ km s^{-1}, $v_s \approx 5.6$ km s^{-1}; bridgmanite: $v_p \approx 11.2$ km s^{-1}, $v_s \approx 6.3$ km s^{-1} at 23.4 GPa and 1850 K), the kinetically inhibited growth of ringwoodite and the abundance of garnet results in a low-velocity layer above the 660 km discontinuity of $\Delta v_p \approx -5\%$, $\Delta v_s \approx -7\%$ (Figs 4 and 5). The low-velocity layer above the lower boundary of the ringwoodite-forming reaction thus increases the *P*- and *S*-wave impedance contrast. When the growth of ringwoodite has reached equilibrium conditions, the profiles of density and seismic wave speeds intersect the profiles of the phase assemblages at thermodynamic equilibrium.

The effects of initial grain size d and mantle upwelling rate v can be described by a kinetic parameter D which is proportional to the upwelling rate and the squared grain size (Dobson & Mariani 2014):

$$D \sim vd^2$$

Scenarios of kinetic inhibition with different initial grain sizes and upwelling rates give the same results if they can be described by the same kinetic parameter. Therefore, the kinetic parameter is an appropriate entity to compare scenarios of kinetically inhibited phase assemblages. Since the kinetic parameter scales with the square of initial grain size d, the kinetic inhibition of ringwoodite is more sensitive to grain size than to upwelling rate. In this study, we set the proportional factor to unity and use

$$D = vd^2$$

in order to compare scenarios of initial grain size d and mantle upwelling rate v.

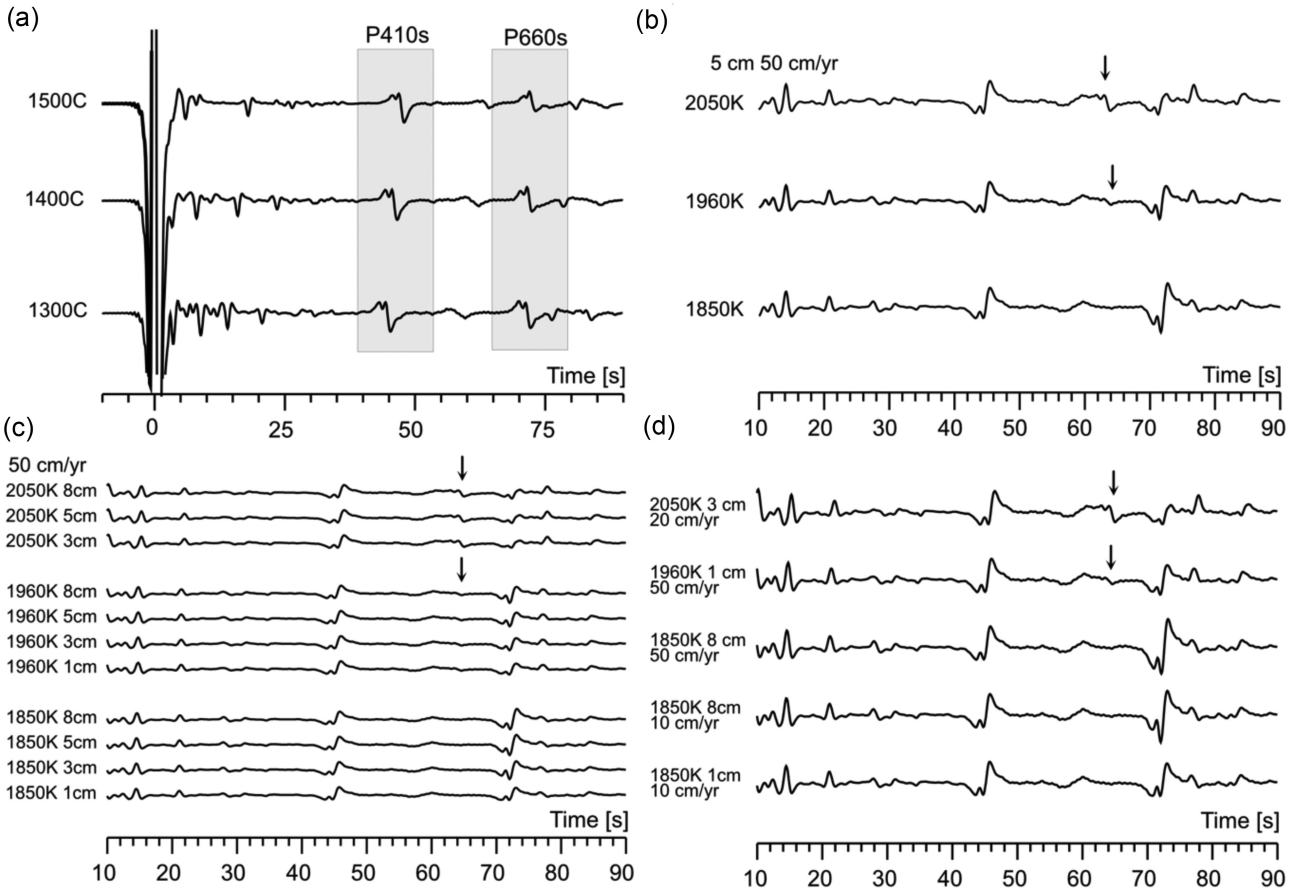

Figure 10: Synthetic waveforms for *P*-to-*S* conversions arriving in the *P*-wave coda with dominant period of 1 s. All traces are recorded at 43° epicentral distance and aligned on the theoretical *P*-wave arrival. All times are given relative to *P*-wave arrival time. (a) Waveforms for pyrolytic models at equilibrium conditions for mantle adiabats with surface potential temperatures ranging from 1300 to 1500 °C. P-to-s conversions from the 410-km discontinuity and the 660 km discontinuity are highlighted. (b) Waveforms for kinetically inhibited transformation for models with 5 cm grain sizes and an upwelling rate of 50 cm yr^{-1} for geotherms at 1850, 1960 and 2050 K. Amplitudes are normalized on the *P*-wave amplitude. Arrows indicate detectable precursors to P660s. (c) Waveforms for kinetically inhibited transformation for 50 cm yr^{-1} upwelling rate and varying temperatures and grain sizes. Amplitudes are normalized on the *P*-wave amplitude. Arrows indicate detectable precursors to P660s. (d) Waveforms for kinetically inhibited transformation for varying temperatures, upwelling rates and grain sizes. Amplitudes have not been normalized and the amplitude variations of the *P*-to-*S* conversion from the ferropericlase and bridgmanite to ringwoodite are observable. Arrows indicate detectable precursors to P660s.

The thickness of the low-velocity layer, that is the depth interval between the onset and the completion of ringwoodite growth, increases exponentially with increasing kinetic parameter of the kinetic parameter (Fig. 5). The exponential behaviour can be explained by the grain growth equation which includes the Arrhenius relation for the reaction rate parameter $k(T)$ (*cf.* eq. 9). For kinetic parameters D between 10 and 100 cm^3 yr^{-1}, kinetic inhibition occurs over a pressure interval of ∼0.1 GPa which is as narrow as the transformation pressure interval of the recombination of ringwoodite from ferropericlase and bridgmanite. A transformation pressure interval of ∼0.1 GPa is equivalent to a low-velocity layer of thickness ∼2 km which is likely below the resolution threshold even of short period PP waves and at the resolution level for receiver function (Ps). Seismic waves therefore sample the reflector and low-velocity layer above in the same way as the reflector for phase assemblages at thermodynamic equilibrium. The onset of seismically detectable kinetic inhibition in terms of the kinetic parameter D is $D > 100$ cm^3 yr^{-1} for 1850 K, $D > 1000$ cm^3 yr^{-1} for 1960 K and $D > 2500$ cm^3 yr^{-1} for 2050 K. The temperature dependence can be explained by the increased diffusion of ions at higher temperatures.

3.2 Synthetic seismograms

We have calculated 1-D synthetic seismograms from the synthetic velocity and density profiles using the reflectivity methods (Fuchs & Müller 1971; Müller 1985) as described in Section 2.4. Here we discuss the effects of the kinematically inhibited velocity structures on PP/SS underside reflections and P-to-s conversions, two probes regularly used for the study of upper mantle discontinuities.

3.2.1 PP and SS precursors

The seismograms calculated for the velocity models with kinetically inhibited recombination reaction of ringwoodite from bridgmanite and ferropericlase are compared to seismograms for velocity models with equilibrated phase assemblages. Using linear vespagrams (Davies *et al*. 1971; Muirhead & Datt 1976), PP/SS and P660P/S660S waveforms are extracted for traveltimes predicted by ak135 (Kennett *et al*. 1995, Fig. 6).

For velocity models where the kinetic inhibition of the ringwoodite growth results in a thicker low-velocity layer of the order of ∼25 km, the PP/SS precursors off the reflector caused by

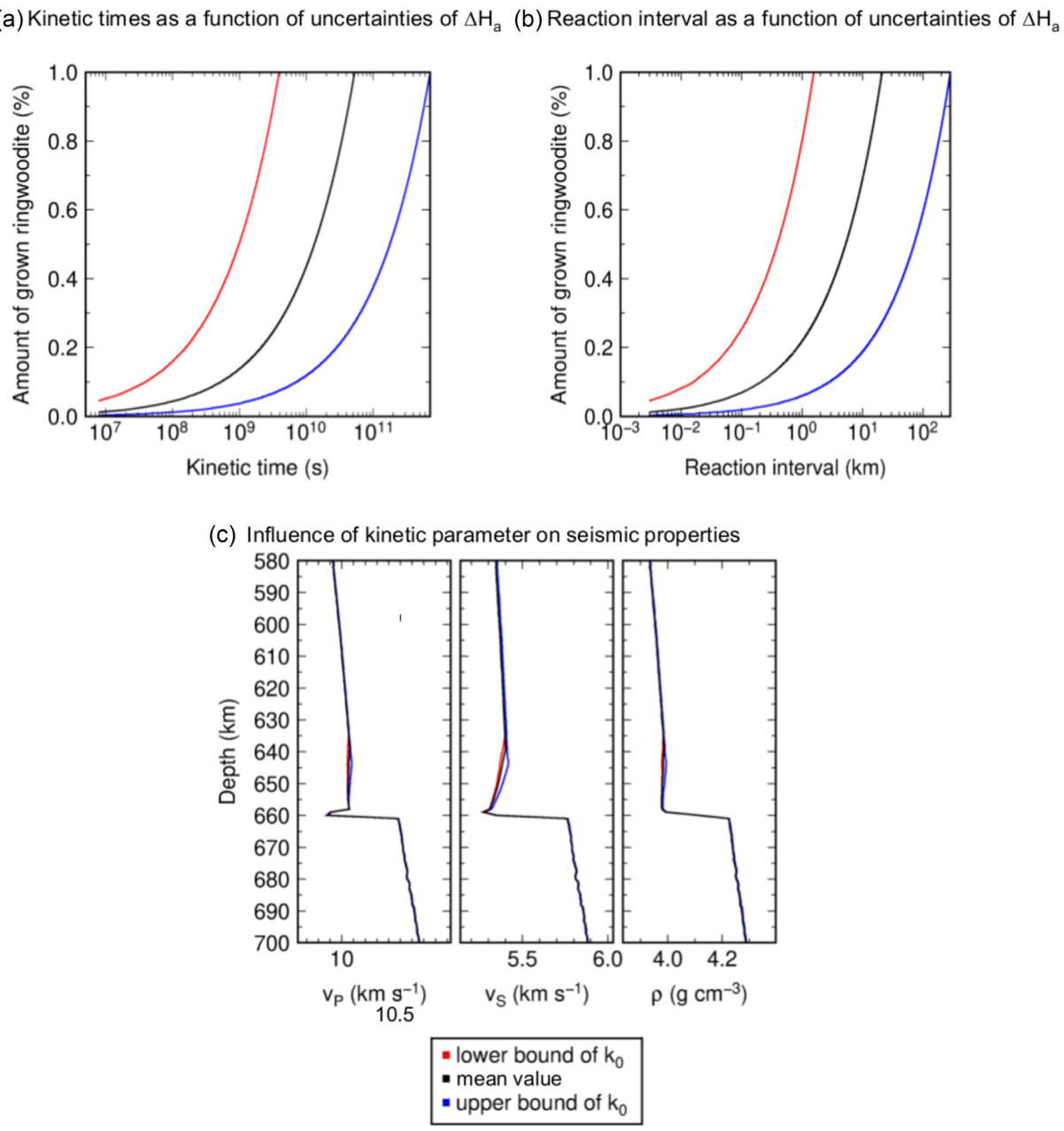

Figure 11: Effects of uncertainties of kinetic parameters on seismic properties of kinetically inhibited phase assemblages and thickness of the low-velocity layer above the onset of ringwoodite growth. The effects have been calculated for an ambient mantle temperature of 1850 K, an initial grain size of 5 cm and an upwelling rate of 50 cm yr^{-1}. (a) Effects of uncertainties of the enthalpy ΔH_a on the growth time of ringwoodite. The red curve denotes the calculation for the lower bound of ΔH_a from Table 3 whereas the blue curve the upper bound of ΔH_a. (b) Effects of uncertainties of the enthalpy ΔH_a on the width of inhibited ringwoodite. (c) Effects of uncertainties of the diffusion coefficient k_0 on the seismic wave speeds and density. The lower and upper bound of k_0 correspond to the uncertainties in Table 3.

kinetically inhibited recombination of ringwoodite are notably advanced for reaction intervals wider than 25 km compared to PP/SS precursors reflected off discontinuities of equilibrated phase transformations (Fig. 3b). The traveltime advances also affect secondary phases of the underside reflections such as depth phases, for example pP660P (Fig. 6). For the kinetic parameters tested here, the maximum traveltime advances for PP underside reflections are ∼0.8 s, whereas maximum traveltime advances for SS underside reflections are ∼1.3 s (Fig. 7). These traveltime residuals correspond to apparent maximum shifts of the discontinuity depth on the order of 5 km.

Amplitudes for PP precursors with a dominant period of 1 s reflected off the kinetically inhibited formation of ringwoodite vary between 120 and 160 per cent relative to the equilibrium model at 1850 K. For the same temperature, amplitudes of SS precursors with a dominant period of 5 s range between 120 and 160 per cent relative to the equilibrium model. The precursor amplitudes for the kinetically inhibited phase assemblages decrease with increasing periods (Fig. 8). The transition from enhanced to apparently unaltered precursor amplitudes is at a dominant period of 5 s for PP and 10 s for SS. Moreover, the PP and SS precursor amplitudes increase with increasing kinetic parameters and increasing thickness of the

low-velocity layer. The PP/SS precursors off the lower boundary of the phase transformation are less affected by interference with PP/SS precursors off the gradient above the low-velocity layer.

While it appears that underside reflections of PP waves at the ringwoodite to bridgmanite plus ferropericlase transition are more difficult to detect than the corresponding SS underside reflection (Estabrook & Kind 1996), there is evidence for P660P waves in some regional studies (e.g. Deuss *et al*. 2006; Thomas & Billen, 2009; Schmerr & Thomas, 2011, Saki *et al*. 2015) and usually the amplitudes of observed P660P waves are smaller than predicted by PREM or a pyrolytic mantle. There is also a noted discrepancy between the detection of P660P and its equivalent underside reflection of PKPPKP (P'660P') (Day & Deuss, 2013). The scarcity of P660P detections in recorded data can likely be explained by compositional and thermal effects that are not captured in our modelling and the assumed pyrolytic starting model (Lessing *et al*. 2015; Guo & Zhou *et al*. 2020; Waszek er al., 2021).

Underside reflection of PP from the 660 km phase transition are rarely detected in recorded data although such detections exist (Deuss *et al*. 2006; Day & Deuss 2013).

The finite width of the low-velocity layer (Fig. 3a) and the vertical resolution of the seismic waves lead to a frequency-dependent behaviour of P660P/S660S precursor amplitudes (Fig. 9). PP waves with 1 s dominant period appear to resolve the increased P wave impedance contrast off the reflector caused by the kinetically inhibited recombination of ringwoodite. The increased P wave impedance contrast results in increased PP precursor amplitudes compared to the reflections for equilibrated phase assemblages. If the dominant period is increased, PP precursor amplitudes off the reflector with kinetic inhibition decrease and have similar PP precursor amplitudes off the reflector as those without kinetic inhibition.

3.2.2 P-to-s conversions (P receiver functions)

Examples of the synthetic waveforms for the kinetically inhibited models and pyrolitic models at equilibrium conditions are shown in Fig. 10. For varying temperatures at equilibrium, we observe strong conversions from the 660 km discontinuity and other discontinuities (e.g. 410- km as well as shallower) with minor waveform and amplitude variations. We calculated synthetics for dominant periods of 0.5, 1 and 2 s and observe very minor variability of the results. While absolute traveltimes for *P*- and *P*-coda arrivals vary, differential traveltime variations are minor, with 0.2 and 0.6 s for the 1960 and 2050 K simulations, respectively, compared to the 1850 K simulations. Waveform variations are limited to larger moveout for a deeper transition, arriving 5.1–8.9 s after P660s.

For the kinetically inhibited transformations we observe strong waveform variations with temperature, where the waveforms of the high temperature models show a dominant precursor about 7 s preceding the arrival from P660s (Figs 10b and c). The precursor due to the low velocity zone will lead to a likely detectable negative polarity precursor in *P*-wave receiver functions (see Fig. S1 for an additional velocity profile at 2050 K). Those detectable negative polarity precursors have been reported in some up-flowing regions of the mantle (e.g. Negi *et al*. 2022). We observe amplitude variations dependent on grain size, upwelling rate, and temperature (Fig. 10d). Amplitudes vary between 52 and 122 per cent relative to the equilibrium model at 1960 K with the smallest amplitudes observed for the highest temperatures. Interference effects lead to apparent inverted waveforms for the P-to-s conversion relative to *P*. Both amplitude and waveform variations for these models would be large enough to be observed in receiver function analyses.

Traveltimes relative to *P* vary slightly for the different models. We observe traveltime variations of ± 0.3 s relative to the equilibrium model at 1960 K. While detectable, these might be difficult to detect for recorded data due to the 3-D velocity variations known to exist in upper mantle.

4 DISCUSSION

4.1 Estimates of uncertainties

The effects of initial grain size and upwelling rate on the seismic properties of kinetically inhibited phase assemblages have been investigated in Section 3.1. Among the kinetic input parameters, that is kinetic rate parameter k_0, reaction enthalpy ΔH_a and temperature T, uncertainties of the reaction enthalpy predominantly affect the seismic properties of kinetically inhibited phase assemblages (Figs 11a and b). Dobson & Mariani (2014) measure the enthalpy of the reaction with an uncertainty of ± 40 kJ mol^{-1} for the ringwoodite layer (Table 1). Varying the enthalpy of the reaction with this value while keeping remaining parameters constant in eq. (9) results in variations of the growth time of ringwoodite until equilibrium conditions by one order of magnitude (Fig. 11b).

Converting growth time into the thickness of the reaction interval using the upwelling rate gives uncertainties of the reaction interval of one order of magnitude. Given the uncertainty of the enthalpy of the reaction for the ringwoodite layer, the reaction interval could therefore range from 1 to ~250 km for kinetic parameters ranging from 1 to 10 000 cm^3 yr^{-1}. On the one hand, reaction intervals with a width of 1–10 km are close to the vertical resolution of PP and SS precursors (e.g. Schmerr & Thomas 2011; Thomas & Billen 2009) and it might be challenging to discriminate kinetic effects from other influences on reaction intervals. On the other hand, reaction intervals with widths of 100–200 km would give increased PP and SS precursor amplitudes due to the increased *P*-wave and *S*-wave impedance contrast and due to the more gradual change of seismic properties from the low-velocity region relative to seismic properties at thermodynamic equilibrium. P-to-s conversions at the discontinuities beneath the receiver typically show higher resolution and are likely able to detect even the thinner layers inferred for the smaller kinetic parameters. Thicker reaction intervals would result in strongly reduced amplitudes of Ps. Reaction intervals of 100–200 km would also affect phase transformations at smaller pressures/shallower depths, for example the wadsleyite to ringwoodite transition, as well as the phase transformations from pyroxene to garnet and from garnet to calcium silicate perovskite. The kinetics of the olivine to wadsleyite phase transition (Poirier 1981; Brearley *et al*. 1992; Kirby *et al*. 1996) and of pyroxene to garnet (Hogrefe *et al*. 1994) have been studied for harzburgitic mantle composition so far. However, kinetic data of other phase transformations in the transition zone are necessary to allow for consistent treatment of kinetic effects on seismic properties within and above the transition zone.

The reaction rate constant k_0 has a minor effect on the seismic properties of the kinetically inhibited phase assemblage (Fig. 11c). *P*- and *S*-wave velocity vary by ± 0.05 km s^{-1}, and density is changed by ± 0.02 g cm^{-3} for varying k_0 to its lower and upper bounds. The thickness of the low-velocity layer above the 660 km discontinuity shifts by ± 4 km.

4.2 Seismological and geodynamic implications

Patterns of mantle flow and dynamics have been investigated using seismic wave speed anomalies in seismic tomography models (e.g. Li *et al*. 2008; Ritsema *et al*. 2011) and seismic waves sampling the upper mantle and mantle transition zone discontinuities using receiver functions (e.g. Vinnik 1977; Farra & Vinnik 2000; Rondenay 2009), short period P'P' reflections (e.g. Niazi & Anderson 1965; Vidale & Benz 1993; Day & Deuss 2013), and PP and SS precursors (e.g. Shearer 1991; Deuss 2009). Since the upper mantle and mantle transition zone discontinuities are sensitive to thermal variations due to their Clapeyron slopes (Bina & Helffrich 1994; Helffrich 2000; Weidner & Wang 2000), variations of discontinuity depth and of transition zone thickness (i.e. the depth between the 410 and 660 km discontinuity) and constraints from mineral physics, are frequently used to infer thermal variations in the mantle (e.g. Ritsema *et al*. 2009; Shearer 2000).

The investigation of reaction kinetics of the reaction from ferropericlase and bridgmanite to ringwoodite can add further constraints on mantle temperature and flow patterns. The effect of kinetic inhibition can be compared to seismic data using a two-step approach. In a first step, through forward modelling of synthetic seismograms for a range of temperatures, upwelling rates and grain sizes. Relevant temperatures can be determined from adiabatic mantle geotherms (Brown & Shankland 1981; Spiliopoulos 1984; Ita & Stixrude 1992; Cobden *et al*. 2008) to estimate excess temperatures (e.g. Sleep 1990; Schilling 1991; Herzberg *et al*. 2007). Heat flux estimates (e.g. Sleep 1990; Courtillot *et al*. 2003) can be converted into estimates for upwelling rates using convection models for vertical upwellings. A steady-state axisymmetric plume with temperature-dependent viscosity might serve as a starting point for estimates of upwelling rates as a function of heat flux and excess temperatures (Loper & Stacey 1983; Schubert *et al*. 2001). In a second step, the seismic recordings can be compared to the set of synthetic seismograms and those models are taken which give the best match with regard to frequency dependent traveltime residuals and amplitude ratios. The set of matching models gives the range of corresponding grain sizes and upwelling rates.

Considering the effects of reaction kinetics of ferropericlase and bridgmanite to ringwoodite on the amplitudes and traveltimes may offer additional constraints on mapping mantle flow using P-to-s receiver functions. P-to-s conversions typically have higher frequencies (Li *et al*. 2000; Wölbern *et al*. 2006). Several studies (van der Meijde *et al*. 2003; Schmandt 2012; Huckfeldt *et al*. 2013) show frequency dependent behaviour of P-to-s conversions at mantle transition zone discontinuities. We see little frequency dependence of P-to-s conversion in our synthetic models within the range typically used for receiver functions, but observe strong waveform variations that are likely to be observable in recorded data as well as strong amplitude variations and small traveltime variations that might add additional constraints for detecting regions with mantle upstreams.

The analysis of PP and SS precursors might have some resolution limitations with respect to the scale of the mantle upwellings which might hamper the detection of the predicted waveforms. Geodynamic modelling indicates that deep thermal mantle plumes have typical diameters of ∼200 km (e.g. Sleep 1990; Schubert *et al*. 2001; Steinberger & Antretter 2006) whereas thermochemical plumes might have larger diameters ranging from 600 to 800 km (Farnetani 2005; Farnetani & Hofmann 2010; Stockmann *et al*. 2019). Lessing *et al*. (2015) use the 2.5-D axisymmetric finite difference technique PSVaxi (Jahnke 2008; Thorne *et al*. 2013) to examine the effects of topography of the upper mantle discontinuities imaged by PP underside reflections with dominant periods of 2 s. Their models show that the PP wavefield reflected off a locally elevated 660 km with a diameter of 200–400 km does not differ significantly from the PP wavefield reflected off a flat reflector at 660 km depth. The size of the detailed topography of the perturbed reflector is smaller than the PP Fresnel zone at 660 km depth and thus might not be resolved. The detection of effects of the kinetically inhibited reaction from ferropericlase and bridgmanite to ringwoodite might therefore be challenging in narrow mantle upwellings. Although conduction might lead to thermal halos around narrow mantle plumes the effect might be small (Sleep 2004) and might not influence the detectability of the plume using underside reflection. Nonetheless, recent tomographic images show that plumes might be broad upstreams (French & Romanowicz 2015), very different to early numerical and laboratory plume experiments which might make the upstream detectable seismically. The pooling of plume material beneath the 660 km discontinuity due to the endothermic phase transition might lead to larger scale temperature anomalies in the region of plume-like mantle upstreams (Tackley *et al*. 1994; Schubert *et al*. 1995; Stockmann *et al*. 2019). Possible candidates for upwellings with large, detectable lateral dimensions are large transient domes near the mantle transition zone (Courtillot *et al*. 2003; Davaille *et al*. 2005; Kumagai *et al*. 2007, 2008). The transient domes are characterized by upwelling rates slower than deep mantle plumes due to their small buoyancy ratio (ratio of chemically driven buoyancy to thermally driven buoyancy). Nonetheless, the transient domes could have excess temperatures up to 300 K in their centre and form a thermal boundary layer with the ambient mantle (Davaille *et al*. 2005). Upwelling mantle material might pond beneath the 660 km discontinuity when encountering the phase transformation from bridgmanite and ferropericlase to ringwoodite (e.g. Schubert & Turcotte 1975; Schubert & Tackley 1995; Tackley 1995; Steinbach & Yuen 1997; Brunet & Yuen 2000; Davaille *et al*. 2005; Farnetani & Samuel 2005). Due to the negative Clapeyron slope, the transformation pressure of the warmer material is shifted towards lower pressure, resulting in a negative buoyancy force which delays further upwelling. The material starts to pond beneath the phase transformation (Davaille *et al*. 2005) and spreads laterally, growing with dimensions broader than plume conduits (e.g. Steinbach & Yuen 1997; Davaille *et al*. 2005; Stockmann *et al*. 2019).

Furthermore, the viscosity contrast across the 660 km discontinuity (e.g. Mitrovica & Forte 2004) might support lateral mantle flow beneath the discontinuity. The geodynamic models of Tosi & Yuen (2011) show additional evidence for horizontal flow whose scale is governed by the viscosity contrast due to temperature variations. For small values of the viscosity contrast, broad and highly viscous plumes are generated that tend to pass through the transition zone relatively unperturbed. For higher values of the viscosity contrast ($10^2 \leq \Delta\eta_T \leq 10^3$), the geodynamic simulations show horizontal channel flows beneath the 660 km discontinuity which might extend up to 1500 km horizontally before tilting to more vertical flow. Therefore, lateral mantle flow could change the fine-scale seismic structure at ∼660 km depth in a way that could allow for the detection of the effects of kinetically inhibited growth with seismic methods sensitive to upper mantle discontinuity structure.

This study has predicted effects of kinetically inhibited growth of ringwoodite in mantle upstreams and the expected effect on seismic probes for discontinuity structure. We find that the effect on PP/SS underside reflection traveltimes is small; amplitudes, although harder to assess in recorded data, might show a larger response to the altered discontinuity structure. For P-to-s conversions

traveltime effects are minor but waveforms and amplitudes of conversions are notably affected. Potentially P-to-s receiver function could be a suitable probe to detect kinetic effects in the phase transitions and to map out mantle flow.

5 CONCLUSIONS

The effects of reaction kinetics of bridgmanite and ferropericlase to ringwoodite in upwelling mantle on elastic properties were investigated using data of kinetic experiments and internally self-consistent thermodynamic modelling. As the kinetic experiments show, growth of ringwoodite is initiated at ferropericlase grain boundaries and is kinetically inhibited due to the necessary diffusion of chemical components. At the initiation of ringwoodite growth, bridgmanite transforms into metastable garnet. Ringwoodite grows from the metastable assemblage of ferropericlase and pyrope-bearing garnet.

The results of the analysis of kinetically inhibited transformation at ∼660 km depth predict possible effects of kinetically inhibited growth of ringwoodite on seismic data which can be summarized as follows:

(i) The increased amount of ferropericlase and garnet results in a localized low velocity zone of $\Delta v_P \sim -5\%$, $\Delta v_S \sim -7\%$ directly above the 660 km seismic discontinuity due to the lower seismic velocities and density of ferropericlase and garnet compared to ringwoodite and bridgmanite. The impedance contrasts for *P* and *S* waves are thus increased compared with seismic velocity profiles of an equilibrated pyrolite mineral assemblage.

(ii) The effects of reaction kinetics on the seismic fine structure at ∼660 km depth depend on the product of the squared grain size and upwelling rate. The change of seismic properties correlates with the product of squared grain size and upwelling rate. Modelling 1-D synthetic seismograms using the seismic profiles of kinetically inhibited phase assemblages show travel time delays of 0.4–0.8 s for PP precursors and delays of 1.2–1.6 s for SS precursors for kinetic inhibition of the ringwoodite-forming reaction. The finite width of the low-velocity layer above the seismic discontinuity results in frequency dependent behaviour of PP and SS underside reflection amplitudes, with higher amplitudes for 1–3 s PP waves and 5–8 s SS waves. However, high-frequency PP and SS waves are rarely observed and the predicted traveltime differences are of similar magnitude as typical picking uncertainties. Hence, it might be challenging to utilize PP and SS underside reflections in order to observe kinetic effects.

(iii) Synthetic seismograms for P-to-s converted waves for velocity models for kinetically inhibited transformations predict strong waveform variations for higher temperature models and amplitude variations dependent on temperature, grain size and upwelling rate. Traveltime variations are maximum ±0.3 s relative to models at equilibrium for temperature of 1960 K. Receiver functions therefore might be a suitable seismic probe to look for kinetic effects on the seismic structure of the 660 km discontinuity in mantle upwellings. A future re-evaluation of P-to-s receiver functions at mantle upwellings would be necessary to study the predicted effects described in this paper.

(iv) Possible candidates for mantle upwellings where reaction kinetics may become important are transient domes with low buoyancy ratios and large lateral dimensions, or broader scale plume upwellings. Material stalling at the phase transformation of bridgmanite and ferropericlase to ringwoodite might generate structure in the resolution range of P-to-s converted waves.

ACKNOWLEDGMENTS

We are grateful for the constructive reviews by the editor Ian Bastow and two anonymous reviewers that helped to greatly improve the quality of the manuscript. We thank Jamie Connolly for assistance with the Perple_X program package (Connolly, 2005). Data analyses were carried out with SeismicHandler (Stammler 1993). Figures were produced with Generic Mapping Tools (GMT, Wessel & Smith 1995). SL was supported under grant DFG TH1530/2–1. The high-pressure kinetic experiments were largely performed at the Bayerisches Geoinstitut under the aegis of an EU large-scale facility grant to D. Rubie and an Alexander von Humboldt Foundation to DD. The Al-free experiment was performed at the ETH Zurich during a visiting professorship by DD. We acknowledge funding from NERC (grants NE/L006898 and NE/L007363). LC was supported under grant DFG TH1530/5–1.

DATA AVAILABILITY

The resulting data of this work and sources code developed during this work are not publicly available. Except the results from kinetic experiments by Dobson & Mariani (2014), data are based on tools available in the public domain:

(i) Perple_X program package (Connolly 2005), utilizing the elastic and thermodynamic properties and the solid solution model of Stixrude & Lithgow-Bertelloni (2011).

(ii) 1-D synthetic seismic modelling using the reflectivity method (Fuchs & Müller 1971) and data processing with seismic waveform analysis tool SeismicHandler (Stammler 1993).

(iii) If you are interested in detailed data, please contact the corresponding author.

REFERENCES

Allègre, C. J. & Turcotte, D. L., 1986, Implications of a two-component marble-cake mantle. *Nature,* **323**(6084), 123–127.

Ballmer, M.D., Lourenço, D.L., Hirose, K., Caracas, R. & Nomura, R., 2017. Reconciling magma-ocean crystallization models with the present-day structure of the Earth's mantle, *Geochem. Geophys. Geosys.,* **18**(7), 2785–2806.

Benz, H.M. & Vidale, J.E., 1993. Sharpness of upper-mantle discontinuities determined from high-frequency reflections, *Nature,* **365**(6442), 147–150.

Bina, C.R. & Helffrich, G., 1994. Phase transition Clapeyron slopes and transition zone seismic discontinuity topography, *J. geophys. Res.: Solid Earth,* **99**(B8), 15853–15860.

Brearley, A. J., Rubie, D. C. & Ito, E., 1992, Mechanisms of the transformations between the α, β and γ polymorphs of Mg_2SiO_4 at 15 GPa. *Phys.Chem. Miner.,* **18**(6), 343–358.

Brown, J. M. & Shankland, T. J., 1981. Thermodynamic parameters in the Earth as determined from seismic profiles, *Geophys. J. R. astr. Soc.,* **66,** 579–596.

Brunet, D. & Yuen, D. A., 2000, Mantle plumes pinched in the transition zone, *Earth planet. Sci. Lett.,* **178,** 13–27.

Cobden, L., Goes, S., Cammarano, F. & Connolly, J. A. D., 2008, Thermochemical interpretation of one-dimensional seismic reference models of the upper mantle: evidence for bias due to heterogeneity, *Geophys. J. Int.,* **175,** 627–648.

Connolly, J. A. D., 2005, Computation of phase equilibria by linear programming: a tool for geodynamic modeling and its application to subduction zone decarbonation, *Earth planet. Sci. Lett.,* **236,** 524–541.

Courtillot, V., Davaille, A., Besse, J. & Stock, J., 2003, Three distinct types of hotspots in the Earth's mantle, *Earth planet. Sci. Lett.,* **205**(3-4), 295–308.

Davaille, A., Stutzmann, E., Silveira, G., Besse, J. & Courtillot, V., 2005, Convective patterns under the Indo-Atlantic box, *Earth planet. Sci. Lett.,* **239,** 233–252.

Davies, D., Kelly, E. & Filson, J., 1971, Vespa process for analysis of seismic signals *Nat.-Phys. Sci.,* **232,** 8–13.

Day, E. A. & Deuss, A., 2013, Reconciling PP and P'P' precursor observations of a complex 660 km discontinuity, *Geophys. J. Int.,***194,** 834–838.

Deuss, A., 2009, Global observations of mantle discontinuities using SS and PP precursors, *Surv. Geophys.,* **30,** 301–326.

Deuss, A., Redfern, S.A., Chambers, K. & Woodhouse, J.H., 2006. The nature of the 660-kilometer discontinuity in Earth's mantle from global seismic observations of PP precursors, *Science,* **311**(5758), 198–201.

Dobson, D. P. & Mariani, E., 2014, The kinetics of the reaction of majorite plus ferropericlase to ringwoodite: implications for mantle upwellings crossing the 660 km discontinuity, *Earth planet. Sci. Lett.,* **408,** 110–118.

Durand, S., Chambat, F., Matas, J. & Ricard, Y., 2012, Constraining the kinetics of mantle phase changes with seismic data. *Geophys. J. Int.,* **189**(3), 1557–1564.

Dziewonski, A. M. & Anderson, D. L., 1981, Preliminary Reference Earth Model, *Phys. Earth planet. Inter.,* **25,** 297–356.

Estabrook, C. & Kind, R., 1996. The nature of the 660-kilometer upper-mantle seismic discontinuity from precursors to the PP phase, *Science,* **274**(5290), 1179–1182.

Farber, D. L., Williams, Q. & Ryerson, F. J., 1994, Diffusion in Mg_2SiO_4 polymorphs and chemical heterogeneity in the mantle transition zone. *Nature,* **371**(6499), 693–695.

Farnetani, C. G. & Samuel, H., 2005, Beyond the thermal plume paradigm, *Geophys. Res. Lett.,* **32,** doi:10.1029/2005GL022360.

Farnetani, C.G. & Hofmann, A. W., 2010, Dynamics and internal structure of the Hawaiian plume, *Earth planet. Sci. Lett.,* **295**(1–2), 231–240.

Farra, V. & Vinnik, L., 2000. Upper mantle stratification by P and S receiver functions, *Geophys. J. Int.,* **141**(3), 699–712.

Fei, H., Faul, U. & Katsura, T., 2021. The grain growth kinetics of bridgmanite at the topmost lower mantle, *Earth planet. Sci. Lett.,* **561,** doi:10.1016/j.epsl.2021.116820.

French, S. W. & Romanowicz, B. 2015. Broad plumes rooted at the base of the Earth's mantle beneath major hotspots. *Nature,* **525**(7567), 95–99.

Fuchs, K. & Müller, G., 1971, Computation of synthetic seismograms with the reflectivity method and comparison with observations, *Geophys. J. R. astr. Soc.,* **23,** 417–433.

Fukao, Y., Obayashi, M. & Nakakuki, T., Deep Slab Project, 2009. Stagnant slab: a review. *Ann. Rev. Earth planet. Sci.* **37,** 19–46.

Fukao, Y., Widiyantoro, S. & Obayashi, M., 2001, Stagnant slabs in the upper and lower mantle transition region, *Rev. Geophys.,* **39,** 291–323.

Gasparik, T., 1996a, Diopside-jadeite join at 16-22 GPa, *Phys. Chem. Mineral.,* **23,** 476–486.

Gasparik, T., 1996b, Melting experiments on the enstatite-diopside join at 70-224 kbar, including the melting of diopside, *Contrib. Mineral. Petrol.,* **124,** 139–153.

Guo, Z. & Zhou, Y, 2020, Finite-frequency imaging of the global 410- and 660-km discontinuities using SS precursors, *Geophys. J. Int.,* **220**(3), 1978–1994.

Helffrich, G. R., 2000, Topography of the transition zone seismic discontinuities, *Rev. Geophys.,* **38,** 141–158.

Herzberg, C., Asimov, P. D., Arndt, N., Niu, Y., Lesher, C. M., Fitton, J.G., Cheadle, M. J. & Saunders, A. D., 2007, Temperatures in ambient mantle and plumes: constraints from basalts, picrites, and komatiites, *Geochem. Geophys. Geosys.,***8,** doi:10.1029/2006GC001390.

Hill, R., 1965, Continuum micro-mechanics of elastoplastic polycrystals, *J. Mech. Phys. Solids,***13,** 89–101.

Hirose, K., 2002, Phase transitions in pyrolitic mantle around 670-km depth: implications for upwelling of plumes form the lower mantle, *J. geophys. Res.,* **107**(B4), ECV 3–1-ECV 3-13.

Hofmann, A. W. & Hart, S. R.(1978). An assessment of local and regional isotopic equilibrium in the mantle. *Earth planet. Sci. Lett.,* **38**(1), 44–62.

Hogrefe, A., Rubie, D. C., Sharp, T. G. & Seifert, F., 1994, Metastability of enstatite in deep subducting lithosphere, *Nature,* **372,** 351–351.

Huckfeldt, M., Courtier, A.M. & Leahy, G.M., 2013. Implications for the origin of Hawaiian volcanism from a converted wave analysis of the mantle transition zone. *Earth planet. Sci. Lett.,* **373,** 194–204.

Irifune, T., Nishiyama, N., Kuroda, K., Inoue, T., Isshiki, M., Utsumi, W., Funakoshi, K., Urakawa, S., Uchida, T., Katsura, T. & Ohtaka, O., 1998, The postspinel phase boundary in Mg_2SiO_4 determined by in situ X-ray diffraction, *Science,* **279,** 1698–1700.

Ita, J. & Stixrude, L., 1992, Petrology, elasticity and composition of the mantle transition zone, *J. geophys. Res.,* **97**(B5), 6849–6866.

Jahnke, G., 2008, Methods for seismic wave propagation on local and global scales with finite differences, *PhD thesis,* Ludwig Maximilians-Universität München, Germany.

Kellogg, J. B., Jacobsen, S. B. & O'Connell, R. J., 2002, Modeling the distribution of isotopic ratios in geochemical reservoirs. *Earth planet. Sci. Lett.,* **204**(1), 183–202.

Kennett, B. L. N., Engdahl, E. R. & Buhland, R., 1995, Constraints on seismic velocities in the Earth from travel-times, *Geophys. J. Int.,* **122,** 108–124.

Kirby, S. H., Stein, S., Okal, E. A. & Rubie, D. C., 1996, Metastable mantle phase transformations and deep earthquakes in subducting oceanic lithosphere, *Rev. Geophys.,* **34,** 261–306.

Korenaga, J., 2005. Firm mantle plumes and the nature of the core–mantle boundary region. *Earth planet. Sci. Let.,* **232,** 29–37.

Kubo, T., *et al.*, 2002, Mechanisms and kinetics of the post-spinel transformation in Mg_2SiO_4, *Phys. Earth planet. Inter.,* **129,** 153–171.

Kubo, T., Ohtani, E., Kato, T., Kondo, T., Hosoya, T., Sano, A. & Kikegawa, T., 2008, Kinetics of the post-garnet transformation: implications for density and rheology of subducting slabs, *Phys. Earth planet. Inter.,* **170,** 181–192.

Kumagai, I, Davaille, A., Kurita, K. & Stutzmann, E., 2008, Mantle plumes: thin, fat, successful, or failing? Constraints to explain hot spot volcanism through time and space, *Geophys. Res. Lett.,* **35**(16), doi:10.1029/2008GL035079.

Kumagai, I., Davaille, A. & Kurita, K., 2007, On the fate of thermally buoyant mantle plumes at density interfaces, *Earth planet. Sci. Lett.* **254,** 180–193.

Langrand, C., Andrault, D., Durand, S., Konôpková, Z., Hilairet, N., Thomas, C. & Merkel, S., 2019, Kinetics and detectability of the bridgmanite to post-perovskite transformation in the Earth's D ″layer. *Nat. Commun.,* **10**(1), 1–9.

Lessing, S., Thomas, C., Saki, M., Schmerr, N.C. & Vanacore, E., 2015, On difficulties of detecting PP precursors, *Geophys. J. Int.,* **201**(3), 1666–1681.

Li, C., van der Hilst, R., Meltzer, A. S. & Engdahl, E. R., 2008, Subduction of the Indian lithosphere beneath the Tibetan Plateau and Burma, *Earth planet. Sci. Lett.,* **274,** 157–168.

Li, X., Kind, R., Priestley, K., Sobolev, S. V., Tilmann, F., Yuan, X. & Weber, M., 2000, Mapping the Hawaiian plume conduit with converted seismic waves, *Nature,* **405**(6789), 938–941.

Loper, D. E. & Stacey, F. D., 1983, The dynamical and thermal structure of deep mantle plumes, *Earth planet. Sci. Lett.,* **33,** 304–317.

Mitrovica, J. & Forte, A. M., 2004, A new inference of mantle viscosity based upon joint inversion of convection and glacial isostatic adjustment data, *Earth planet. Sci. Lett.,* **225,** 177–189.

Muirhead, K. & Datt, R., 1976, N-th root process applied to seismic array data, *Geophys. J. R. astr. Soc.,* **47**(1), 197–210.

Müller, G., 1985, The reflectivity method: a tutorial, *J. Geophys.,* **58,** 153–174.

Negi, S. S., Kumar, A., Ningthoujam, L. S. & Pandey, D. K. 2022. Mapping the mantle transition zone beneath the Indian Ocean geoid low from Ps receiver functions. *Tectonophysics,* **831,** 229330. https://doi.org/10.1016/J.TECTO.2022.229330

Niazi, M. & Anderson, D.L., 1965. Upper mantle structure of western North America from apparent velocities of P waves, *J. geophys. Res.,* **70**(18), 4633–4640.

Poirier, J. P., 1981, On the kinetics of olivine-spinel transition, *Phys. Earth planet. Inter.,* **26**(3), 179–187.

Putnis, A. 1992. *An Introduction to Mineral Sciences*. Cambridge Univ. Press.

Reuss, A., 1929, Berechnung der Fließgrenze von Mischkristallen auf Grund der Konstanten des Einkristalls, *Z. Angew. Math. Mech.,* **9,** 49.

Ringwood, A. E., 1969, Phase transformations in the mantle, *Earth planet. Sci. Lett.,* **5,** 401.

Ritsema, J., Deuss, A., van Heijst, H. J. & Woodhouse, J. H., 2011, S40RTS: a degree-40 shear-velocity model for the mantle from new Rayleigh wave dispersion, teleseismic travel time and normal-mode splitting function measurements, *Geophys. J. Int.,* **184,**(3) 1223–1236.

Ritsema, J., Xu, W., Lithgow-Bertelloni, C. & Stixrude, L., 2009, Estimates of the transition zone temperature in a mechanically mixed upper mantle, *Earth planet. Sci. Lett.,* **277,** 244–252.

Rondenay, S. 2009. Upper mantle imaging with array recordings of converted and scattered teleseismic waves, *Surv. geophys.,* **30**(4), 377–405.

Saki, M, Thomas, C., Nippress, S. & Lessing, S., 2015, Topography of upper mantle seismic discontinuities beneath the North Atlantic: the Azores, Canary and Cape Verde plumes, *Earth planet. Sci. Lett.,* **409,** 193–202.

Saki, M., Thomas, C., Cobden, L., Abreu, R. & Buchen, J., 2019. Causes for polarity reversals of PP precursor waves reflecting off the 410 km discontinuity beneath the Atlantic, *Phys. Earth planet. Inter.,* **286,** 111–126, doi:10.1016/j.pepi.2018.11.007.

Schilling, J-G., 1991, Fluxes and excess temperatures of mantle plumes inferred from their interaction with migrating mid-ocean ridges, *Nature,* **352,** 397–403.

Schmandt, B., 2012, Mantle transition zone shear velocity gradients beneath USArray, *Earth planet. Sci. Lett.,* **355-356,** 119–130.

Schmerr, N. & Thomas, C., 2011, Subducted lithosphere beneath the Kuriles from migration of PP precursors, *Earth planet. Sci. Lett.,* **311,** 101–111.

Schubert, G., Anderson, C. & Goldman, P. 1995. Mantle plume interaction with an endothermic phase change. *J. geophys. Res.,* **100**(B5), 8245–8256.

Schubert, G. & Tackley, P. J., 1995, Mantle dynamics: the strong control of the spinel-perovskite transition at a depth of 660 km, *J. Geodyn.,* **20**(4) 417–428.

Schubert, G., Turcotte, D. L. & Olson, P., 2001, *Mantle Convection in the Earth and Planets,* Cambridge Univ. Press.

Shearer, P. M., 1991, Constraints on upper mantle discontinuities from observations of long-period reflected and converted phases, *J. geophys. Res.,* **96,** 18 147–18 182.

Shearer, P. M., 2000, *Earth's Deep Interior: Mineral Physics and Tomography from the Atomic to the Global Scale,* AGU, 115–131.

Shimojuku, A., Boujibar, A., Yamazaki, D., Yoshino, T., Tomioka, N. & Xu, J., 2014, Growth of ringwoodite reaction rims from $MgSiO_3$ perovskite and periclase at 22.5 GPa and 1,800°C, *Phys. Che. Miner.,* **41,** 555–567.

Sleep, N. H., 1990, Hotspots and mantle plumes: some phenomenology, *J. geophys. Res.,* **95,** 6715–6736.

Sleep, N. H., 2004. Thermal haloes around plume tails. *Geophys. J. Int.,* **156**(2), 359–362.

Solomatov, V.S., 1996. Can hotter mantle have a larger viscosity? *Geophys. Res. Lett.* **23,** 937–940.

Solomatov, V.S., El-Khonzondar, R. & Tikare, V., 2002. Grain size in the lower mantle: constrains from 510 numerical modeling of grain growth in two-phase systems. *Phys. Earth planet. Inter.,* **129,** 265–282.

Spiliopoulos, S., 1984. The Earth's thermal profile - is there a mid-mantle thermal-boundary layer?, *J. Geodyn.,* **1,** 61–77.

Stammler, K., 1993, Seismic handler: programmable multichannel data handler for interactive and automaticprocessing of seismological analysis, *Comput. Geosci.,* **19,** 135–140.

Steinbach, V. & Yuen, D. A., 1997, Dynamical effects of a temperature- and pressure-dependent lower-mantle rheology on the interaction of upwellings with the transition zone, *Phys. Earth planet. Inter.,* **103,** 85–100.

Steinberger, B. & Antretter, M., 2006. Conduit diameter and buoyant rising speed of mantle plumes: Implications for the motion of hot spots and shape of plume conduits, *Geochem. Geophys. Geosys.,* **7**(11).

Stixrude, L. & Lithgow-Bertelloni, C., 2005. Thermodynamics of mantle minerals – I. Physical properties, *Geophys. J. Int.,* **162,** 610–632.

Stixrude, L. & Lithgow-Bertelloni, C., 2011, Thermodynamics of mantle minerals—II. Phase equilibria, *Geophys. J. Int.,* **184,** 1180–1213.

Stockmann, F., Cobden, L., Deschamps, F., Fichtner, A. & Thomas, C., 2019. Investigating the seismic structure and visibility of dynamic plume models with seismic array methods, *Geophys. J. Int.,* **219**(Supplement_1), S167–S194.

Sun, S.S. 1982. Chemical composition and origin of the Earth's primitive mantle, *Geochimica et Cosmochimica Acta,* **46**(2), 179–192.

Sung, C.-M. & Burns, R. G., 1976, Kinetics of high-pressure phase transformations: implications to the evolution of the olivine-spinel transition in the downgoing lithosphere and its consequences on the dynamics of the mantle, *Tectonophysics,* **31,** 1—32.

Tackley, P. J., 1995. On the penetration of an endothermic phase transition by upwellings and downwellings, *J. geophys. Res.,* **100,** 15 477–15 488.

Tackley, P. J., Stevenson, D. J., Glatzmaier, G. a. & Schubert, G. 1994. Effects of multiple phase transitions in a three-dimensional spherical model of convection in Earth's mantle. *J. geophys. Res.,* **99**(B8), 15 877–15 901.

Tackley, P.J., Xie, S., Nakagawa, T. & Hernlund, J.W., 2005, Numerical and laboratory studies of mantle convection: philosophy, accomplishments, and thermochemical structure and evolution, in *Earth's Deep Mantle: Structure, Composition and Evolution,* pp. 83–99, eds Van der Hilst, R., Bass, J.D., Matas, J. & Trampert, J., American Geophysical Union, Washington DC.

Tammann, G., 1920, Über Anlauffarben von Metallen, *Z. Anorg. Allg. Chem.,* **111,** 78.

Thomas, C. & Billen, M., 2009, Upper mantle structure along a profile in the southwest Pacific, *Geophys. J. Int.,* **176,** 113–125.

Thorne, M.S., Garnero, E.J., Jahnke, G., Igel, H. & McNamara, A.K., 2013, Mega ultra low velocity zone and mantle flow, *Earth planet. Sci. Lett.,* **364,** 59–67.

Tosi, N. & Yuen, D.A., 2011, Bent-shaped plumes and horizontal channel flow beneath the 660 km discontinuity, *Earth planet. Sci. Lett.,* **312,** 348–359.

van der Hilst, R.D. & Engdahl, E.R., 1991. On ISC PP and pP data and their use in delay-time tomography of the Caribbean region, *Geophys. J. Int.,* **106**(1), 169–198.

Van der Meijde, M., Marone, F., Giardini, D. & Van der Lee, S., 2003. Seismic evidence for water deep in Earth's upper mantle, *Science,* **300**(5625), 1556–1558.

Vinnik, L., 1977, Detection of waves converted from P to SV in the mantle, *Phys. Earth planet. Inter.,* **15,** 39–45.

Voigt, W., 1928, *Lehrbuch der Kristallphysik,* Teubner.

Wang, Y., Uchida, T., Zhang, J., Rivers, M. L. & Sutton, S. R., 2004. Thermal equation of state of akimotoite $MgSiO_3$ and effects of the akimotoite-garnet transformation on seismic structure near the 660 km discontinuity, *Phys. Earth planet. Inter.,* **143-144,** 57–80.

Waszek, L., Tauzin, B., Schmerr, N.C., Ballmer, M.A. & Afonso, J.C., 2021, A poorly mixed mantle transition zone and its thermal state inferred from seismic waves. *Nat. Geosci.,* **14,** 949–955.

Watson, E. B. & Price, J. D., 2002, Kinetics of the reaction $MgO+Al_2O_3 \rightarrow MgAl_2O_4$ and Al-Mg interdiffusion in spinel at 1200 to 2000°C and 1.0 to 4.0 GPa. *Geochim. Cosmochim. Acta,* **66,** 2123–2138.

Weidner, D. J. & Wang, Y., 2000, Phase transformations: implications for mantle structure, in *Earth's Deep Interior: Mineral Physics and Tomography from the Atomic to the Global Scale, Geophysical Monograph Series,* Vol. **117,** pp. 215–235, eds Karato, S.-I., Forte, A., Liebermann, R., Masters, G. & Stixrude, L., AGU.

Weidner, D.J. & Wang, Y., 1998. Chemical- and Clapeyron-induced buoyancy at the 660 km discontinuity, *J. of geophys. Res.: Solid Earth,* **103**(B4), 7431–7441.

Wessel, P. & Smith, W. H. F., 1995, New version of the Generic Mapping Tools released, *EOS, Trans. Am. geophys. Un.,* **76,** 329.

Wölbern, I., Jacob, A.W.B., Blake, T.A., Kind, R., Li, X., Yuan, X., Duennebier, F. & Weber, M., 2006. Deep origin of the Hawaiian tiltered plume conduit derived from receiver functions. *Geophys. J. Int.* **166,** 767–781.

Yamazaki, D., Inoue, T., Okamoto, M. & Irifune, T. 2005. Grain growth kinetics of ringwoodite and its implication for rheology of the subducting slab. *Earth planet. Sci. Lett.,* **236**(3), 871–881.

Yamazaki, D., Kato, T., Ohtani, E. & Toriumi, M., 1996. Grain growth rates of $MgSiO_3$ - perovskite and periclase under lowermantle conditions, *Science,* **274,** 2052–2054.

SUPPORTING INFORMATION

Supplementary data are available at *GJI* online.

Please note: Oxford University Press is not responsible for the content or functionality of any supporting materials supplied by the authors. Any queries (other than missing material) should be directed to the corresponding author for the paper.